Accurate determination of the chiral indices of individual carbon nanotubes by combining Electron Diffraction and Resonant Raman Spectroscopy

Levshov D.I.[1], Tran H.N.[2], Paillet M. [2], Arenal R. [3,4*], Than X.T. [2, 5], Zahab A. A. [2], Yuzyuk Y.I. [1], Sauvajol J.-L. [2], Michel T. [2 *]

Affiliations

[1] Faculty of Physics, Southern Federal University, Rostov-on-Don, Russia
[2] Laboratoire Charles Coulomb UMR 5221, Université de Montpellier - CNRS F-34095 Montpellier, France
[3] Laboratorio de Microscopias Avanzadas, Instituto de Nanociencia de Aragon, Universidad de Zaragoza, 50018 Zaragoza, Spain
[4] ARAID Foundation, 50018 Zaragoza, Spain
[5] Laboratory of Carbon Nanomaterials, Institute of Materials Science, VAST, Hanoi, Vietnam

Abstract

The experimental approach combining high resolution transmission electron microscopy (HRTEM), electron diffraction (ED) and resonant Raman spectroscopy (RRS) on the same free-standing individual carbon nanotubes (CNT) is the most efficient method to determine unambiguously the intrinsic features of the Raman-active phonons. In this paper, we review the main results obtained by the approach regarding the intrinsic features of the phonons of single-walled (SWNT) and double-walled carbon nanotubes (DWNT). First, we detail the different methods to identify the structure of SWNTs and DWNTs from the analysis of their electron diffraction patterns (EDP). In the following, we remind the principal features of the Raman response of SWNTs, unambiguously index-identified by ED. A special attention is devoted to the effect of the inter-layer interaction on the frequencies of the Raman-active phonons in index-identified DWNTs. The information obtained on index-identified SWNT and DWNT allows us to propose Raman criteria, which help identifying CNT when the ED fails to propose a single assignment. The efficiency of the Raman criteria as the complement to the ED information for the index-assignment of a few SWNTs and DWNTs is shown. The same approach to index-assign a triple-walled carbon nanotube (TWNT), by combining ED and RRS information, is reported.

[*] Corresponding authors. Tel: +33 (0)467 14 35 90. E-mail: thierry.michel@umontpellier.fr, arenal@unizar.es

1. Introduction

Carbon nanotubes (CNT) are among the most promising materials for the modern photonics and optoelectronics [1]. However, due to the strong dependence of their physical properties on the atomic structure (e.g. diameter (d), chiral angle (θ), number of layers) [2], the essential prerequisite for any basic or applied research in the field of carbon nanotubes has become the knowledge of their structural parameters. So far, several approaches for the structure analysis of individual carbon nanotubes have been established. They are based on high-resolution transmission electron microscopy (HRTEM) [3–6], scanning tunneling microscopy [7–9], electron diffraction (ED) [10–17], photoluminescence (PL) [18], Rayleigh spectroscopy [19–21], optical absorption [22], and resonant Raman spectroscopy (RRS) [23–28].

HRTEM and ED are obviously the most powerful methods for the direct structure analysis at the single nanotube level. It was demonstrated, that when used in combination with other techniques, such as Resonant Raman spectroscopy [26], absorption [22,29] or Rayleigh spectroscopy [30], they allow to determine unambiguously intrinsic optical and/or vibrational properties of individual CNTs [29–37]. For instance, the combined application of ED and Rayleigh spectroscopy provided a firm experimental basis for the predicted family variation with nanotube chirality and the splitting of optical transitions in metallic SWNTs, which ultimately played a critical role in guiding spectroscopic assignments [30]. On the other hand, few years ago from Raman experiments performed on individual single-walled carbon nanotubes (SWNT), unambiguously index-identified by electron microscopy techniques, Raman criteria for the SWNT's structure assignments were established [38]. Finally, HRTEM and ED have been successfully combined with mechanical [39], electronic transport [40] and non-linear optics [41] measurements.

This paper is organized as follows: in Section 2 the experimental approach is presented. In Section 3, we give an overview of the electron diffraction techniques and their application to the index-assignment of individual single- and double-walled carbon nanotubes (DWNT). Section 4 presents an overview of the structural information, which can be derived from the analysis of the Raman spectra of SWNTs and DWNTs, namely: the diameter and the electronic nature of each layer and, in addition for DWNT, the inter layer distance. The limits of the diffraction methods in some specific situations are discussed in section 5. Especially, we show that in some cases such as low-quality electron diffraction pattern (EDP) due to the nanotube vibrations under the electron beam, or EDP distortion due to the high tilt angle between the electron beam and the axis of the nanotube, or, on the other hand, the intrinsic complexity of the DWNT with large diameters or/and

the same chirality of layers, the ED approaches fail to give unambiguous index-assignments. In section 5, we also illustrate the efficiency of Raman spectroscopy as a tool for the index-assignment of individual DWNT in the situations where electron diffraction fails to provide such assignment. Finally, in section 6 we test the complementarity between ED and Raman spectroscopy on a more complex system than DWNT, namely a triple-walled carbon nanotubes (TWNT), for which ED results alone fails providing an unambiguous index-assignment.

2. Experimental approach

Figure 1 displays a sketch of the combined measurements performed on the same suspended individual CNT. There are mainly two advantages in the presented experimental configuration: (i) the environment is minimized (substrate or surfactant is not interacting with the nanotube), and (ii) the CNT is accessible by electron and laser beams. The major issue of the sample fabrication is to acquire CNTs that are long enough to be suspended over holes or slits (as large as several tens of microns).

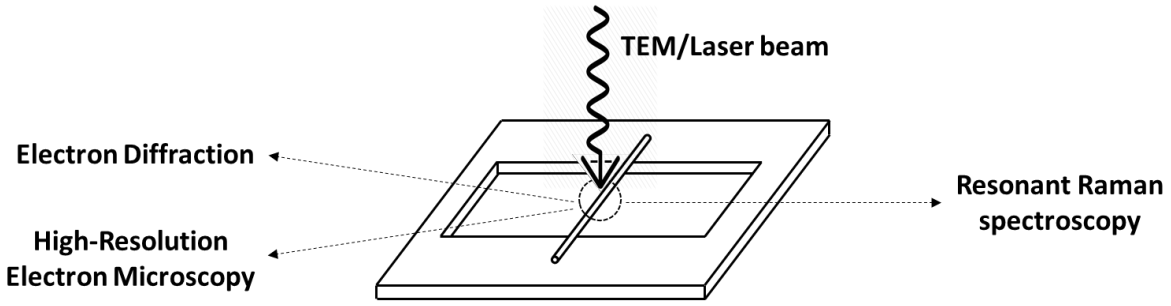

Figure 1: Schematic illustration of the experimental design. Individual free-standing (suspended) carbon nanotubes are directly grown on commercial perforated silicon nitride TEM grids (hole diameters ~ 2 µm) or across home-made slits on SiO_2/Si_xN_y substrates (slit width ~ 50 µm). This design enables the combination of HRTEM imaging, electron diffraction, and Raman scattering to, respectively, probe the structural, vibrational and electronic properties of the same individual carbon nanotubes.

In most of the studies discussed in this paper, the ultra-long individual single-, double- and triple-walled carbon nanotubes were grown by the catalytic chemical vapor deposition (CCVD) method directly on the commercial perforated silicon nitride TEM grids or across home-made slits fabricated by wet-etching of a SiO_2/Si or Si_xN_y/Si wafers. Typical growth parameter are reported in references [15,42,43]. As it was confirmed by high-resolution electron microscopy, electron diffraction and resonant Raman spectroscopy, the investigated nanotubes are homogenous and preserve their atomic structure all along the length [15].

HRTEM and ED experiments are usually performed at low dose and voltage (typically 80 kV) in order to minimize electron damages on the CNT. HRTEM micrograph alone usually does not permit to derive the structural parameters with a good accuracy, however it gives a fast diagnostic on the number of layers, possible amorphous carbon contamination and bundling effects. On the other hand, Resonant Raman spectroscopy measurements can be performed with standard available setups, though a large number of excitation lasers (including tunable lasers) should be used to improve the determination of the resonance conditions. In all experiments, incident and scattered light polarizations are oriented along the individual nanotubes axis (the so-called (// //) geometry). Finally, the laser power must always be carefully controlled to avoid CNT heating.

3. Index assignment of carbon nanotubes by electron diffraction

We review in this part the main methods used to analyze electron diffraction patterns of individual carbon nanotubes with a special focus on DWNTs.

The atomic structure of a single-walled carbon nanotube may be determined uniquely by a pair of the so-called chiral indices (n, m) [2]. These indices are related to nanotube's diameter and helicity by formulas $d = \sqrt{3}a_{C-C} \cdot \sqrt{n^2 + nm + m^2}/\pi$ and $\theta = arctan\left(m\sqrt{3}/(2n+m)\right)$, where $a_{C\text{-}C}$ = 0.142 nm is carbon-carbon distance in graphene. It is worth mentioning that the helicity or chiral angle θ defines the chirality of the nanotubes (*zig-zag* (θ =0 deg.), *armchair* (θ =30 deg.) and *chiral* (θ between 0 and 30 deg.)). The properties, in particular the electronic and optical ones, depend on this parameter, as well as on the diameter or equivalently on n and m indices.

The atomic structure of a double-walled carbon nanotube is characterized by (n,m) of the constituent SWNTs (called layers in the following) and by convention defined as follows: $(n,m)_{inner}@(n,m)_{outer}$. The average diameter and interlayer distance of a DWNT are then calculated from relations: $<d> = (d_{out} + d_{in})/2$; $\delta r = (d_{out} - d_{in})/2$, where d_{in} and d_{out} are the inner and outer diameters, respectively.

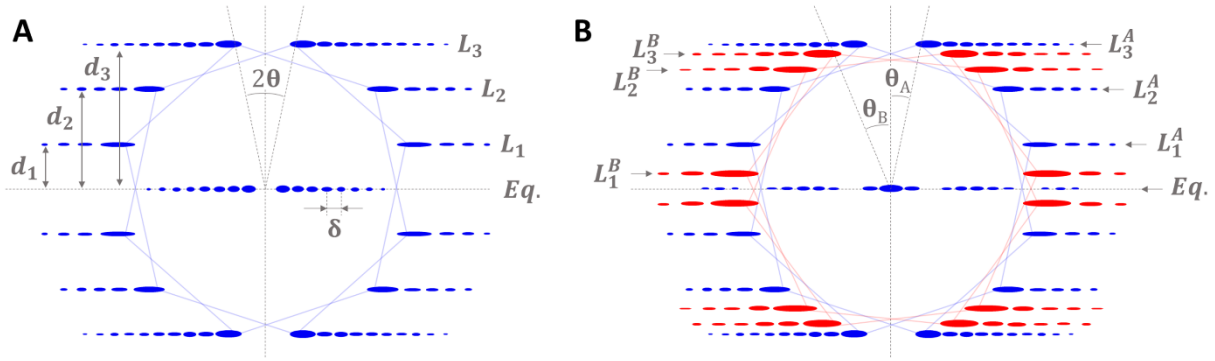

Figure 2: Schematic illustration of an electron diffraction pattern of (A) the chiral single-walled carbon nanotubes (24,7) and (B) double-walled carbon nanotube (13,9)@(24,7). The principal layer lines are denoted as Eq. (equatorial), L_1, L_2 and L_3. The quantities d_1, d_2, d_3 refer to the distances between the equatorial line and the corresponding layer-lines. Red and blue layer lines are associated to the different layers of the DWNT.

The EDP provides a direct way to determine all the CNT structural parameters, e.g. diameters, chiral angles and (n, m) indices. A typical EDP of a chiral single-walled carbon nanotube is shown in the Figure 2A. The exact positions of 12 main reflections in the EDP can be calculated within the kinematical diffraction theory, where SWNT is considered as a series of continuous molecular helixes [16,44–46]. However, in more conceptual and simplistic terms and as a first approximation, one can consider the EDP as arising from electron diffraction from a pair of graphene sheets at the top and bottom sides of the SWNT perpendicular to the incident electron beam. Hence, a pair of hexagonal lattices, rotated by angle 2θ, is seen in the Figure 2A. Due to the finite dimensions of the nanotube, its translational symmetry and 1D periodicity, the hexagons' vertices appear smeared and have an oscillation period proportional to the inverse diameter *d*. By convention, the central oscillating reflex is called an equatorial line (abbreviated Eq. line), while the others are named "layer lines" (1^{st}, 2^{nd}, 3^{rd} or L_1, L_2, L_3 etc.). One defines the distance between the equatorial line and the corresponding layer lines as d_1, d_2 and d_3 and the period of radial oscillations of equatorial line as δ (Fig. 2A). The non-equatorial layer lines observed in a DWNT electron diffraction pattern (see Fig. 2B) is usually regarded as a simple sum of those of constituent SWNTs. One has to define two sets of layer lines for each layer, denoted as L_i^A and L_i^B. On the other hand, due to the interference effects the intensity distribution of the equatorial line of DWNTs is characterized by two oscillation periods e and E, defined as shown in the Figure 3C.

3.1. Review of methods for analyzing electron diffraction patterns

Allen et al. showed, that the existing procedures for EDP treatment of single-walled carbon nanotubes is ambiguous, and each of them cannot be used in isolation (see detailed review in Ref. [47]). They concluded the necessity of combination of different treatment techniques for the

successful index-assignment of SWNTs. In this review, we analyze EDPs of double-walled carbon nanotubes, which have a higher level of complexity for the index-assignment.

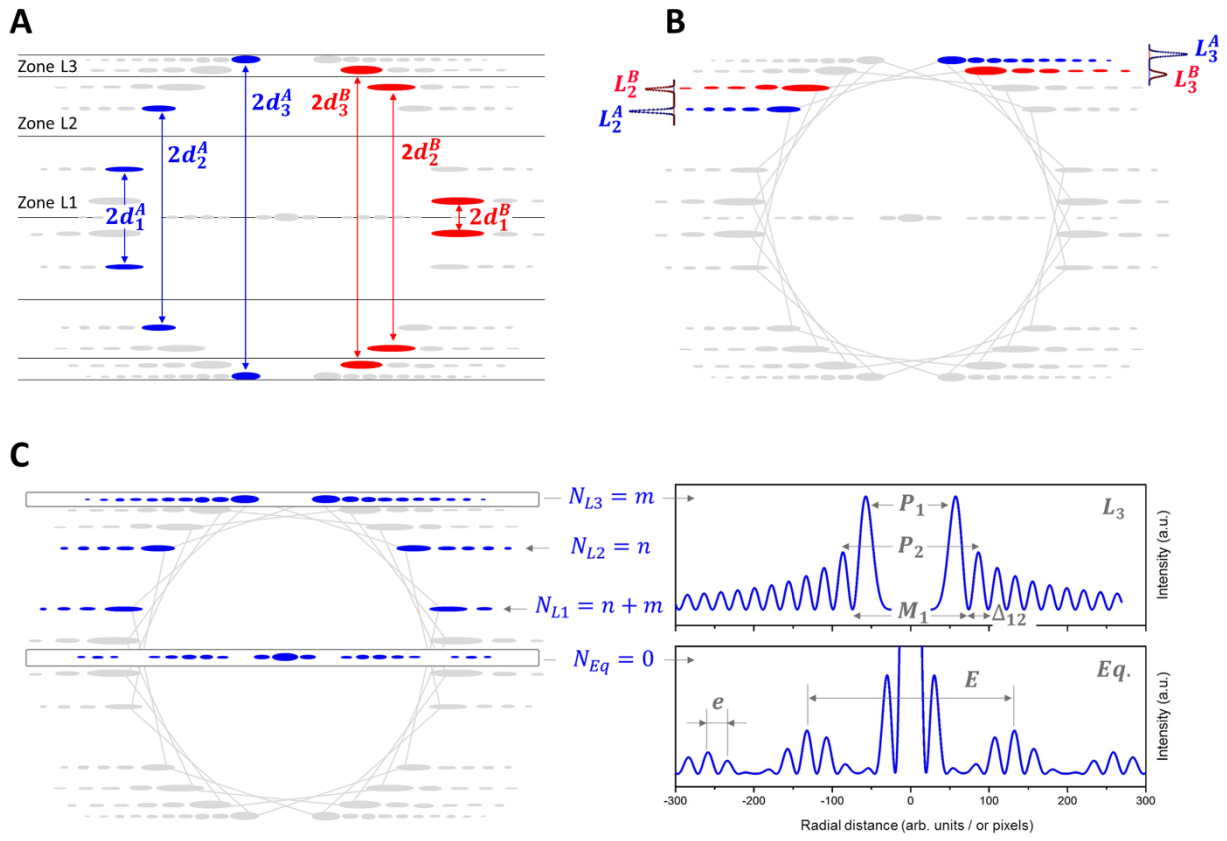

Figure 3. Principal steps of electron diffraction pattern analysis of an individual double-walled carbon nanotube: (A) measurements of axial position d_i of the main layer-lines; (B) comparison of the axial intensity distribution of layer lines; (C) analysis of radial intensity distribution of the main layer-lines, in particular the equatorial line.

Figure 3 summarizes principal steps of the electron diffraction pattern analysis of a chiral double-walled carbon nanotube. The corresponding EDP is sketched in Figure 2B. For the sake of clarity, we color in grey all extra-details that are not pertinent to the information analyzed at each step. The most general procedure includes the measurements of the axial positions of reflections (Fig. 3A), measurements of relative intensity of the layer-lines (Fig. 3B) and the analysis of radial intensity distribution (Fig. 3C). One should note, that the procedure shown in the Fig. 3, can be easily generalized to the case of single-walled nanotubes or multi-walled nanotubes with higher number of layers.

3.1.1 Measuring axial positions of layer-lines

It was shown previously (Fig. 2A), that the EDP of a chiral SWNT has 12 non-equatorial reflections divided into 6 layer-lines. The axial positions, d_i, of these layer-lines can be directly related to the chiral angle θ. On the other hand, the EDP of a chiral DWNT will have twice as many reflections. Hence, to determine θ, one need to group all the reflections in the analyzed EDP according to the correct layer. *A-priori* this grouping is unknown. However, Jiang *et al*. showed that d_2 and d_3 belonging to the same layer of a MWNT should form a conjugated pair [48] with the following property: the bigger d_3, the less is d_2, and vice versa. Based on this principle, Deniz et al. proposed a zone method for the accurate grouping of layer-lines [49]. One can divide reciprocal space of the EDP into three zones as follows: zone L_1 — from 0 to 0.577, zone L_2 — from 0.577 to 1, zone L_3 — from 1 to 1.154, where axial distances are given in terms of the factor 1/a (Fig. 3A); a = 0.2461 nm is the lattice constant of graphene. The reflections from the two limiting cases of *armchair* and *zig-zag* layers will lie on the zone boundaries (see Figure 2 from Ref [49]), while d_1, d_2 and d_3 of a chiral SWNTs will appear only within zones L_1, L_2 and L_3 respectively. Hence, the general rule for the EDP analysis of some multi-walled carbon nanotube is to define the L_i zones and in a step-by-step manner assign d_i by groups using the property of conjugated pairs (the grouping by two sets A and B for a DWNT is shown in the Fig. 3A).

It is clear from the dimensions of each of the zones in Figure 3A, that the layer-lines are not evenly spaced. When the layers of the MWNT have close chiral angles, their L_3 layer-lines may overlap leading to the odd number of reflections in each quadrant. This fact complicates the grouping of reflections. However, in that case one can use another useful relation to discern between closely spaced L_3 lines, namely: $d_3 = d_2 + d_1$.

Finally, we relate the set of measured d_i values to the chiral angle of the particular layer. Since L_3 and L_2 layer lines (from the first reflection order) are the most intense in the EDP, apart the Eq. line, it is reasonable to use them for estimating θ. It is determined in a straightforward way by formula [50]:

$$\theta = arctan\left(\frac{1}{\sqrt{3}}\frac{2d_2 - d_3}{d_3}\right) \qquad (1)$$

Since this relation considers only the ratio of d_i values, it is calibration-free. From the values of d_i one can also deduce the ratio of m/n by the following equation [14]:

$$\frac{m}{n} = \frac{2d_2 - d_3}{2d_3 - d_2} \qquad (2)$$

3.1.2. Measuring relative intensities of layer-lines

Given two groups of layer lines L_i^A and L_i^B (or consequently θ_A and θ_B) identified in the previous step, one can assign them to the inner or outer layers of the DWNT. Due to the different number of atoms in the inner and outer layers, different intensity of layer-lines may be expected. By integrating intensity distribution in the axial directions of two closely-situated layer lines of the same order (as shown in the Figure 3B), one can find that the outer layer would correspond to the layer-line with the highest intensity. As indicated in Figure 3B, the intensities of L_2^A and L_3^A are higher, so they correspond to the outer layer.

3.1.3. Analyzing radial intensity distribution of layer-lines

The intensity distribution of the layer-line in the radial direction can be characterized by the square of a Bessel-function of a particular order (Fig. 3C), related to the (n,m) indices of the nanotube. For instance, L_1, L_2 and L_3 layer-lines have the following Bessel function orders: $N_{L1} = n + m$; $N_{L2} = n$; $N_{L3} = m$, respectively [14]. The order of the oscillations can be determined directly by extracting their radial intensity distribution and its subsequent fit with a Bessel function. Or, simply, by measuring ratios R_1, R_2 and R_3 defined as follows [51]:

$$R_1 = \frac{P_2}{P_1} \qquad R_2 = \frac{P_1}{\Delta_{12}} \qquad R_3 = \frac{M_1}{\Delta_{12}} \qquad (3)$$

where P_1 is the distance between the first two highest maxima, P_2 is the distance between the second two highest maxima, M_1 is the separation between two first symmetrical minima (M_1) and Δ_{12} is the distance between two adjacent minima (see notations on the Fig. 3C). By comparing measured values of R_1, R_2 and R_3 with the theoretical calculations (see Tables in Ref [51]), one can derive the order of the corresponding Bessel function.

The radial oscillations of the equatorial line have $N_{Eq} = 0$ and are of particular interest. In a DWNT EDP, they provide information on the mean diameter <d> and the interlayer distance δr [46]:

$$<d> = \frac{1}{e}; \quad \delta r = \frac{1}{E} \qquad (4)$$

where e and E are the oscillation periods (see right part of the Fig. 3C). In the EDP of a SWNT, one finds diameter $d_0 = 1/\delta$, where δ is the period of oscillations of the equatorial line (Fig. 2A). It should be noted that the use of equations (4) requires the calibration of the diffraction pattern (see for instance Section 3.2.1 of Ref [46]).

Finally, given the axial measurements of d_i and radial measurements of e and E (or δ) one can use the so-called "intrinsic layer lines" method, which allows to directly calculate (n,m) indices and also to estimate the tilt τ of the nanotube in respect to the incoming electron beam [13,52]. One finds (n,m) of a SWNT from the following formulas [13]:

$$n = \frac{\pi}{\sqrt{3}} \cdot (2d_3 - d_2) \cdot \frac{1}{\delta}; \qquad m = \frac{\pi}{\sqrt{3}} \cdot (2d_2 - d_3) \cdot \frac{1}{\delta} \tag{5a}$$

and for $(n_{in},m_{in})@(n_{out},m_{out})$ of a DWNT one has [52] :

$$n_{in} = \frac{\pi}{\sqrt{3}} \cdot (2d_3 - d_2) \cdot \left(\frac{1}{e} - \frac{1}{E}\right); \qquad m_{in} = \frac{\pi}{\sqrt{3}} \cdot (2d_2 - d_3) \cdot \left(\frac{1}{e} - \frac{1}{E}\right) \tag{5b}$$

$$n_{out} = \frac{\pi}{\sqrt{3}} \cdot (2d_3 - d_2) \cdot \left(\frac{1}{e} + \frac{1}{E}\right); \qquad m_{out} = \frac{\pi}{\sqrt{3}} \cdot (2d_2 - d_3) \cdot \left(\frac{1}{e} + \frac{1}{E}\right) \tag{5c}$$

Since these relations consider only ratio of d_i and δ (or d_i and e, E), they are calibration-free.

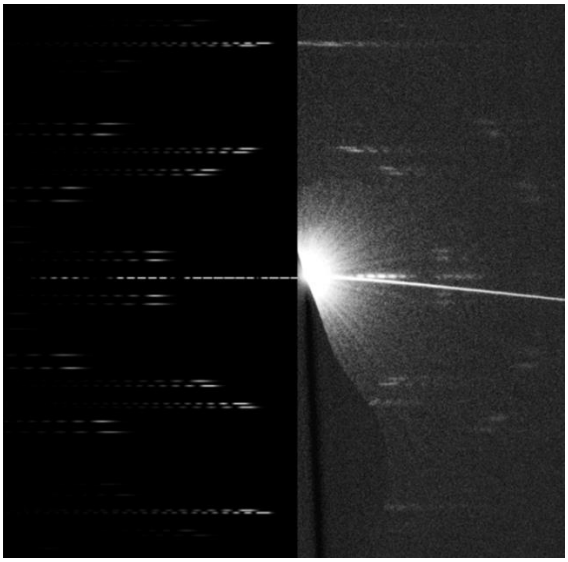

Figure 4: Comparison of simulated (left) and experimental (right) electron diffraction patterns for the index-assignment of an individual double-walled carbon nanotube (22,11)@(27,17). Simulation was performed using code Diffract.

To summarize, three distinct methods for the analysis of the electron diffraction pattern can be found in the literature. The classical method relies on the direct calculation of (d,θ) pair through the relations (1) and (4), followed by a series of simulation procedures [15–17,46,50,53]. A unique structural assignment is then obtained from comparison of the experimental ED pattern with simulated one for all possible structures in a reasonable range. This comparison is shown in Fig. 4. Second method, introduced by Liu and Qin et al. [51,54], analyses the orders of Bessel functions of the main oscillations in the EDP and from them determines the indices n or m of each layer.

The last one was originally developed by Jiang et al. for single-walled nanotubes [13], then optimized for double-walled by Liu et al. [52]. It is based on direct determination of the (n, m) indices from the so-called "intrinsic layer lines". These methods for analyzing the EDP of NTs can also be applied to BNNTs, as well as to other NTs having the same structure [16,55,56].

The application of the above-mentioned methods should be done with care, since their accuracy can be sensitive to different factors. For instance, any tilt τ of the axial plane of a nanotube away from normal to the incident electron beam leads to an increase of the measured d_i distances by a factor of $1/\cos(\tau)$, and also to the change in the radial positions of the peaks in the layer lines [51]. Consequently, it may lead to the wrong index-assignment when using formulas (3) and (5), as will be demonstrated afterwards. Finally, regarding the classical method, the effect of the tilt angle can also alter the (n,m) assignment. To overcome this problem, it was proposed for instance in Ref. [10] to perform simulations of the ED pattern not only by considering different structures, but also different tilt angles in a reasonable range. The comparison with simulations allows to determine the indices and at the same time to measure the incidence angle by varying these parameters in a trial-and-error procedure until the simulated pattern matches the experimental one.

4. Raman criteria for the index assignment of individual nanotubes

Resonant Raman spectroscopy (RRS) is the other powerful method for the probing and indexation of carbon nanotubes [57]. RRS has been extensively used for the characterization of bulk samples of individual SWNTs on the basis of pattern recognition and comparison between experimental and calculated optical transition energies [24,25]. On the other hand, Raman criteria of assignment of the structure of SWNTs based on the features of the main Raman-active modes, namely the radial breathing modes (RBM) and G modes, have been established from measurements performed on index-identified free-standing SWNTs (see Ref. [38] for details). First, we revisit these Raman criteria and discuss their accuracy [27,28,38]. Thereafter, concerning the assignment of the structure of each layer of a DWNT, we report recent Raman results obtained on index-identified DWNTs. On this basis, we propose different criteria, which help to index-assign the layers in DWNTs.

4.1. Raman criteria for the assignment of single-walled carbon nanotubes

In this part, we briefly revisit the most useful Raman criteria which can be used as information to assign the structure of SWNTs. These criteria are based on the dependence as a function of the diameter and chirality of the main features of RBM and G-modes, namely: the

frequency of the RBM, line shape and frequency of G modes, and the resonance conditions of both modes.

4.1.1 The radial breathing mode range

RBM is a Raman active mode where all carbon atoms move in-phase in the radial direction. RBM is a totally symmetric mode, belonging to the A_1 (A_{1g}) symmetry irreducible representation in chiral (achiral) SWNT. RBM appears at low-frequency (examples of RBM are shown on Figure 5, left) and its frequency, $\omega_{RBM}(d)$, was found to be inversely dependent on the nanotube's diameter. Several experimental $\omega_{RBM}(d)$ relations have been established for individual SWNTs, and they all can be summarized by the generic formula [58]:

$$\omega_{RBM} = \frac{227}{d}\sqrt{1 + C_e \cdot d^2} \qquad (6)$$

where C_e parameter is conventionally used to express different environmental conditions around the nanotube [58,59]. Note that several experimental papers have reported the relationships:

$$\omega_{RBM} = \frac{A}{d} + B$$

It should be emphasized that, in a limited range of diameters, the previous relations are equivalent.

Different values of C_e, A and B have been experimentally obtained for various types of samples, as for examples in individual SWNTs dispersed in D_2O and surrounded with a surfactant: A=214.4 cm^{-1} nm and B=18.7 cm^{-1} [24], or A=223 cm^{-1} nm and B=10 cm^{-1} [25].

More striking, different values of C_e were obtained from measurements on individual free-standing, and then assumed as environment-free, SWNTs. Liu et al. experimentally find a value of C_e equal to 0 [60] in agreement with the theoretical predictions [61–64]. By contrast, a value of C_e = 0.065 nm^{-2} was derived from experiments performed on a series of individual free-standing index-identified SWNTs [26,65,66]. These two dependencies of the RBM frequency versus the nanotube diameter are summarized on the Figure 5.

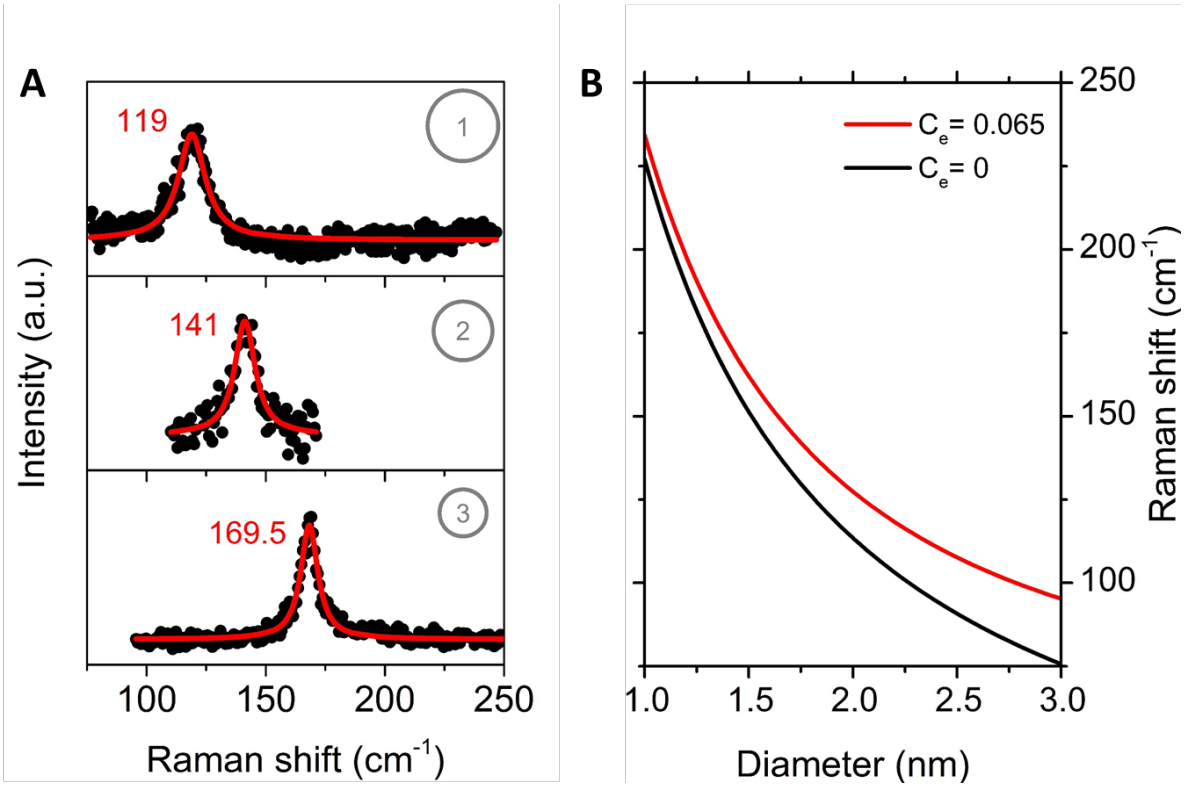

Figure 5: (A): RBM region of Raman spectra measured on index-identified SWNTs. #1 – (27,4), #2 –(17,9), #3 –(10,10). Black dots are experimental data, red lines are Lorentzian fit. (B): *Comparison between two relationships* $\omega_{RBM}(d)$ *established from measurements performed on individual free-standing index-identified SWNTs.*

These significant differences illustrate the high sensitivity of a free-standing SWNT on its environment. For a free-standing SWNT the environment is mainly the surrounding atmosphere. It was established recently that, at ambient conditions, water molecules can form a cylindrical adsorption layer around individual SWNT [67,68]. In experiments performed on individual free-standing SWNTs at room temperature and in air, the vibrational coupling between the surrounding adsorption layer and individual SWNTs via van der Waals interaction is the most probable origin of the presence of a non-zero additional term (see Fig.3 of Ref.[67]).

In summary, measurements of the RBM frequency can be used as a tool to estimate the diameters of individual SWNTs. However, the experimental conditions, including the environmental conditions, have to be precisely defined in order to make the right choice of the C_e coefficient in the expression (6). The use of a bad $\omega_{RBM}(d)$ relation has a dramatic consequence on the accuracy of the diameter measurements, especially at large diameters. For instance, considering the two extreme relations displayed on the Figure 5, for an experimental frequency of 200 cm^{-1} the diameter is in the range 1.12-1.18 nm (average diameter: 1.15 ± 0.03 nm) and for a frequency of 100 cm^{-1} the diameter is in the range 2.25-2.77 nm (average diameter: 2.5± 0.3 nm).

By contrast, when the C_e coefficient is known, the estimation of the diameter of a SWNT via the measurement of its RBM frequency is straightforward.

4.1.2 The G modes range

The G modes of single-walled carbon nanotubes correspond to the totally symmetric tangential vibrations of carbon atoms originating from the iTO and iLO degenerated modes of graphene (E_{2g} symmetry) [69]. G-modes are observed at high frequency, typically in the 1500-1600 cm^{-1} range. In agreement with symmetry considerations [70], for a chiral SWNT two components (G+ and G-) of A_1 symmetry are observed (Fig. 6A), while only one (A_{1g} symmetry) for an achiral SWNT (Figure 3 of the Ref. [28]).

The profile of each component strongly depends on the metal vs. semiconducting nature of the tube. In a *chiral semiconducting* SWNT, the profiles of both G modes are narrow and symmetric. They are described by a lorentzian line shape (Figure 6A, top). It is well established that the frequency of the G- component, assigned to the TO G mode, strongly depends on the tube diameter [28]. The G+ component, assigned to the LO G mode, is located typically around 1590 cm^{-1} for tube diameter in the 1.2 - 2.4 nm range [38,71]. In the case of *chiral metallic* SWNTs, the G- profile becomes broad and is usually represented by the Breit–Wigner–Fano (BWF) lineshape (Figure 6A, bottom) [72]. The position of the broad low-frequency component depends on the diameter. The narrow high-frequency G+ component is observed typically around 1590 cm^{-1}. The high- and low-frequency components are assigned to the TO and LO G modes respectively (opposite to the semiconducting nanotubes) [73,74]. Finally, in *armchair* and *zigzag* SWNTs a single component is Raman-active: the transverse optical (TO) and longitudinal optical (LO) G mode, respectively.

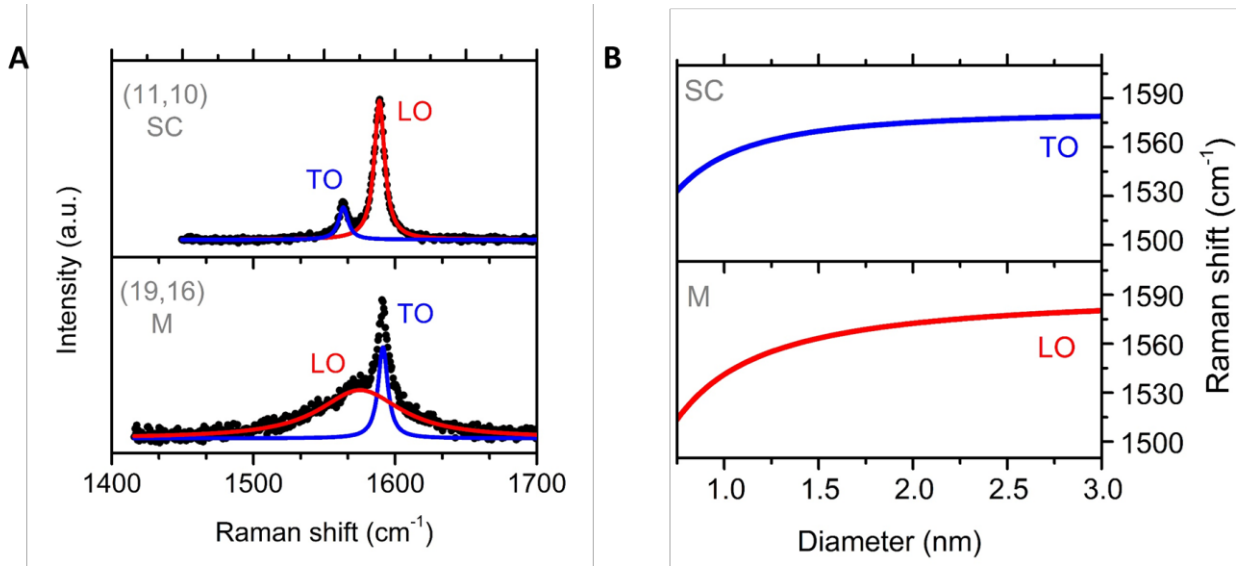

Figure 6: (A) The profile of G modes for a chiral semiconducting (top) and a chiral metallic

(bottom) SWNT, (B) diameter dependence of the average frequency of TO mode in semi-conducting SWNT (blue solid line) and that of LO mode in metallic SWNT (red line).

The diameter dependence of the frequencies of the TO mode of semiconducting SWNT was derived from measurements on sorted SWNT suspensions with well-defined chirality [71]:

$$\omega_{TO}(d) = 1582 - \frac{27.5}{d^2} \qquad (7)$$

This relation is in good agreement with those found from measurements on individual free-standing SWNTs [38].

On the other hand, the experimental diameter dependence of the frequencies of the LO mode of metallic SWNT (expression 8) fits very well with the one predicted by calculations [73,75].

$$\omega_{LO}(d) = 1582 - \frac{38.8}{d^2} \qquad (8)$$

Both previous relations are plotted in Figure 6B. It should be emphasized, that these relations cannot permit to evaluate with a good accuracy the diameter of semiconducting and metallic SWNT, especially at large diameter. However, a fair agreement between measured and expected values for a given tube diameter should be found *a posteriori* to confirm the *(n,m)* assignment. Finally, one can notice that the equations (7) and (8) remain valid even when individual free-standing SWNTs are exposed to the different environments such as water molecules [68], since for this case mainly van der Waals interaction is expected between the molecules and the nanotube wall (contrary to the case where the nanotube is doped by charge or energy transfer).

In summary, the number of components of the G band, measured in the (// //) polarized Raman spectrum, permits to identify the chiral or achiral character of an individual suspended SWNT (see Table 1). A number of components greater than two unambiguously identify the CNT as a bundle or a multi-walled nanotube. On the other hand, the measurement of a broad low-frequency component unambiguously identifies the SWNT under investigation as metallic [28]. However, it must be emphasized that this later criterion fails in the case of metallic armchair tube for which only the TO mode is Raman-active. As expected for a TO mode, the corresponding component is narrow and symmetric.

Nanotube	# of components	G-band profile	G-	G+
Semiconducting chiral	2	LO and TO: narrow & symmetric	TO	LO
Metallic chiral	2	LO: broad & asymmetric TO: narrow & symmetric	LO	TO
Armchair	1	narrow and symmetric	-	TO
Semiconducting *zigzag*	1	narrow and symmetric	-	LO
Metallic *zigzag*	1	broad and asymmetric	LO	

Table 1. Summary of the different G-band profiles depending on the nature of the single-walled nanotubes (see text for details).

Finally, it must be emphasized that quantum interference effects can lead to a drastic enhancement of one of the components (G- or G+) with regards to the other one and consequently to the bad assignment of the nature of the investigated nanotube (for instance, achiral instead of chiral) [76].

4.1.3 The optical transition energies

The measurement of the complete Raman spectrum of individual carbon nanotubes is only possible when the laser energy E_L is in resonance or quasi-resonance with one of the transition energies, E_{ii}, of the nanotubes. This resonance condition allows us to evaluate with reasonable accuracy the transition energies of the single nanotube under investigation. The transition energies can be more precisely determined from the measurements of the resonant Raman excitation profiles (REP) [24,25,77,78].

Concerning transition energies measured in SWNT, it was possible to define a normalized "Kataura" plot (E_{ii} vs. d) [38,65] from the matching between experimental transitions energies, E_{ii}, measured by the Raman resonance conditions on index-identified SWNTs, and the rigidly shifted [79,80] transition energies, E_{NTB}, calculated within non-orthogonal tight-binding approach [81]. This normalized "Kataura" plot permits to predict the energy transitions of free-standing SWNTs measured in air (Figure 7). Consequently, when the Raman spectrum of an individual free standing SWNT is measured at a given laser excitation energy, the comparison with the transitions of the normalized "Kataura" plot permits to propose its most probable index assignments. It is worth noticing that when several laser energies are used the accuracy of this index assignment is greatly improved.

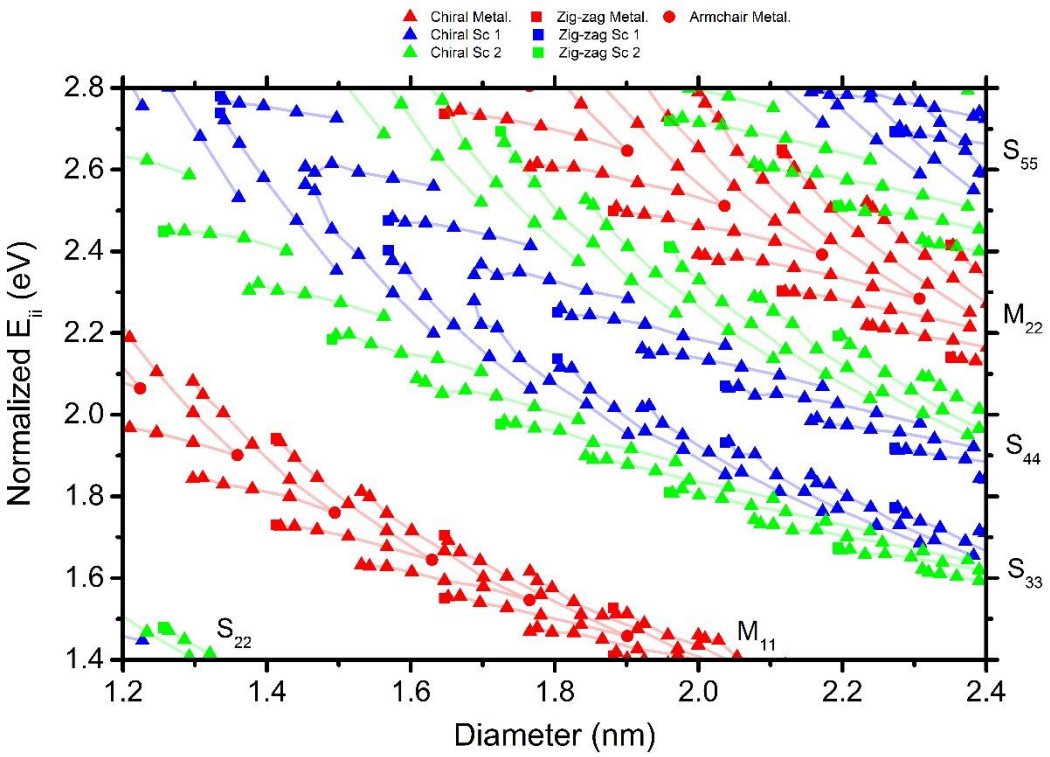

Figure 7: Part of the renormalized "Kataura" plot (adapted from Ref. [79]*). S_{ii} (M_{ii}) define the order of optical transitions energies E_{ii} for semiconducting (metallic) SWNTs.*

4.2. Raman criteria for the assignment of double-walled carbon nanotubes

A DWNT is a more complex system than a SWNT. However, it is also the simplest model to study the mechanical and electronic interactions between concentric carbon layers. The diameter of each layer as well as the inter-layer distance plays an essential role in the properties of DWNTs.

The intrinsic features of Raman-active modes of DWNTs have been recently investigated from Raman experiments performed on index-identified DWNTs [31,33–36,82]. The effect of the interlayer distance on the strength of the mechanical coupling between the layers, and thus on the frequencies of the Raman-active modes, have been studied. By contrast with SWNTs, the relation between the frequencies of the Raman modes and the diameters of the constituting layers is not straightforward. Consequently, the establishment of Raman criteria based on the frequencies of the Raman modes is not easy, and, at this stage, only few Raman qualitative criteria can be proposed as the help to identify the structure of a DWNT.

4.2.1 The radial breathing-like mode range

In individual double-walled carbon nanotubes, two modes are observed in the low-frequency range. They were assigned to in-phase and out-of-phase radial collective breathing vibrations of the constituent SWNT layers and called radial breathing-like modes (RBLM). Their frequencies depend on the mechanical coupling between the inner and outer tubes [29,34]. It was shown experimentally [31,34] that an up-shift of both in-phase and out-of-phase RBLM in comparison with RBMs of individual constituent SWNTs is expected. More importantly, it was established that the shift depends not only on diameters, but also on the inter-layer distance between concentric layers.

Figure 8 summarizes the dependence of the RBLMs on diameter and interlayer distance recently obtained from measurements on index-identified DWNTs. It is confirmed that RBLMs are upshifted with respect to the RBMs of the constituent SWNTs (the values of the shifts are given in parentheses in the Figure 8). On the other hand, we clearly observe that: (i) for close inter-layer distances, both RBLM downshift when the average tube diameters increase (Fig. 8, vertical direction); (ii) for close average tube diameters, and an interlayer distance larger than 0.335 nm (close to the equilibrium distance in graphite), the out-of-phase RBLM downshifts when the interlayer distance increases (Fig. 8, horizontal direction).

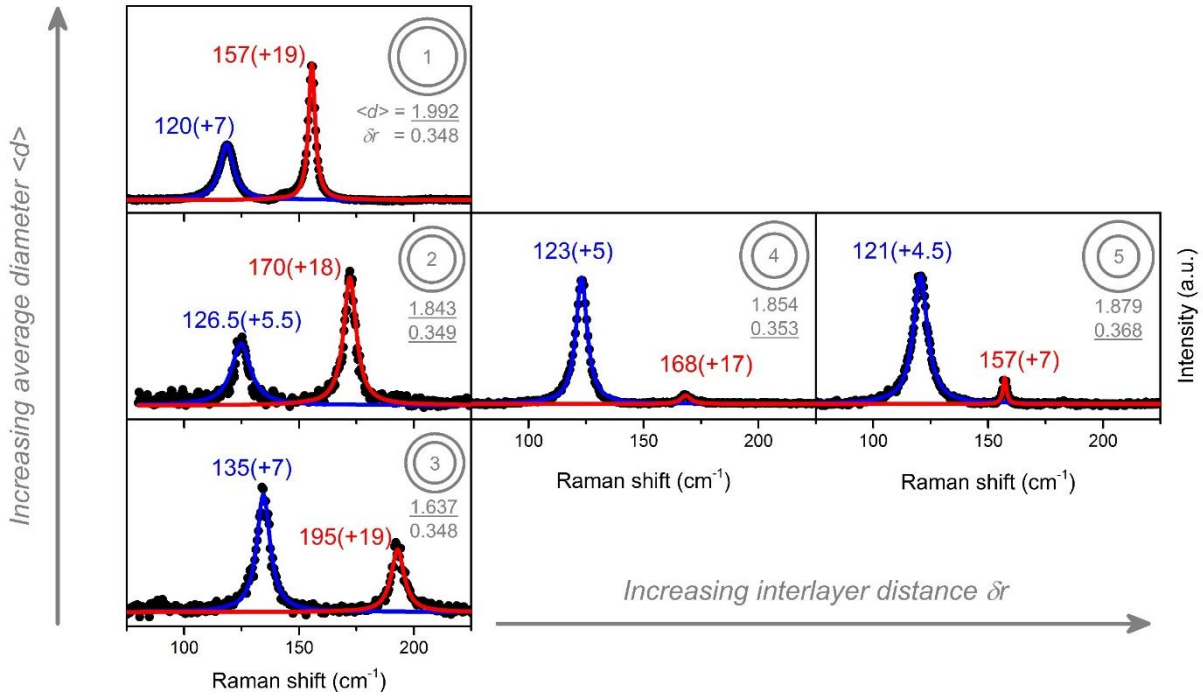

Figure 8: RBLM region of the Raman spectra of different DWNTs. (vertical direction) diameter dependence of the RBLM for DWNTs with close inter-layer distances: #1–(15,9)@(22,12), #2–(18,2)@(20,12), #3 –(10,9)@(18,11); (horizontal direction) inter-layer

distance dependence of the RBLM for DWNTs with close average diameters: #2–(18,2)@(20,12), #4 – (13,9)@(24,7), #5 – (14,8)@(19,14). The shifts of the RBLM with respect to the RBM frequencies of constituent SWNT are given in parentheses.

Opposite to SWNTs in which a single and direct relationship between RBM frequencies and diameters has been established, such relation does not exist for RBLM in DWNTs.

Different models of van-der-Walls coupled harmonic oscillators were developed in order to predict the dependence of the RBLM frequencies on the diameters of the inner and outer layers, associated to a given inter-layer distance [34,64].

In the simplest approach, using the notations of Liu and co-workers [34], the frequencies of the in-phase (ω_L) and out-of-phase (ω_H) RBLMs are given by:

$$\omega_L = \frac{1}{2\pi c} \cdot \omega_c \cdot \sqrt{\frac{1}{2}\left[(z_1 + z_2) - \sqrt{(z_1 - z_2)^2 + 4}\right]} \qquad (9a)$$

$$\omega_H = \frac{1}{2\pi c} \cdot \omega_c \cdot \sqrt{\frac{1}{2}\left[(z_1 + z_2) + \sqrt{(z_1 - z_2)^2 + 4}\right]} \qquad (9b)$$

where $z_1 = \frac{\omega_i^2}{\omega_c^2} + \sqrt{\frac{m_o}{m_i}}$, $z_2 = \frac{\omega_0^2}{\omega_c^2} + \sqrt{\frac{m_i}{m_o}}$, $\omega_c^2 = \frac{k_c}{\sqrt{m_i m_o}}$, $\omega_i^2 = \frac{k_i}{m_i}$, $\omega_o^2 = \frac{k_o}{m_o}$,

m_i and m_o are inner-layer and outer-layer unit-length mass respectively and they are determined from the knowledge of the diameters of inner and outer SWNTs which are directly related to their chiral indices (n_i,m_i) and (n_o, m_o) respectively. The unit-length intrinsic force constant k_i (k_o) for inner (outer) constituent SWNT can be accurately determined from the individual radial breathing mode (RBM) frequency-diameter relationship. It should be emphasized that in order to derive k_i (k_o) the RBM frequency-diameter relations adapted to the experimental environment of each layer have to be used (see 4.1.1. paragraph). For instance, in [34] both ω_i and ω_o are given by $\omega_{i(o)}$ $=228/d_{i(o)}$(nm). In [31], the frequency of the RBM of the inner tube is given by $\omega_i = 228/d_{in}$(nm) and that of the outer tube by $\omega_o = 228 /d_{out}$ (nm) $(1+C_e d_{out}^2)^{1/2}$, with C_e=0.065 nm^{-2} arising from the interaction of the outer-wall with the ambient atmosphere.

The only unknown parameter in equations 9a and 9b is the unit-length coupling force constant, k_c, which characterizes the van-der-Waals interaction between the two concentric carbon layers. For any given DWNT, defined by a couple of diameters (d_o, d_i), one can reproduce the in-phase (ω_L) and the out-of-phase (ω_H) RBLM frequencies by using a single value of k_c. The unit-length coupling force constant, k_c, can be approximated using the average unit-area inter-layer van-der-Waals potential U_{vdw} as:

$$k_c = \frac{\partial^2 U_{vdw}}{\partial r^2}\ \pi\ \frac{(d_{out} + d_{in})}{2} \qquad (10)$$

where ($\partial^2 U_{vdw}/\partial r^2$) is the unit-area force constant.

The dependence of ($\partial^2 U_{vdw}/\partial r^2$) on the inter-walls distance was first established by Liu et al. from measurements on index-identified DWNTs [34] and recently completed [35]. This dependence is displayed in Figure 9 (adapted from the Figure 3d of Ref. [34]).

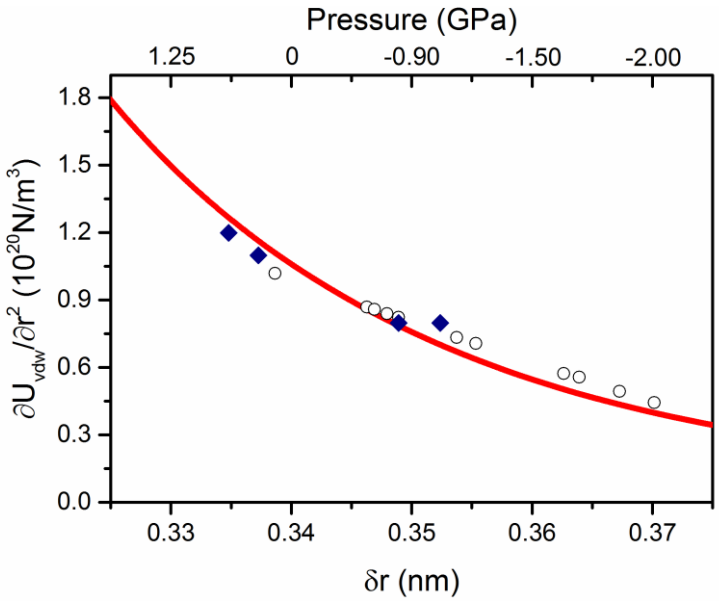

Figure 9: Unit-area force constant, $\partial^2 Uvdw/\ \partial r^2$, owing to tube–tube van-der-Waals interaction. Open dots are experimental data from [34]*; diamonds are experimental data from* [35]*. The red line is a polynomial expression which fits the dependence of van der Waals interaction between unit-area graphene sheets under pressure obtained from compressibility measurements of graphite* (Ref [83]*) and extrapolated for distance larger than 0.34 nm.*

On Figure 9, the values of $\partial^2 U_{vdw}/\partial r^2$ derived from the fits of the RBLM frequencies of index-identified DWNTs (Figure 9, symbols) are compared with a polymonial expression which fits the van der Waals interaction between unit-area graphene sheets under pressure obtained from compressibility measurements of graphite (Ref [83]) and extrapolated for distance larger than 0.34 nm (red line in Figure 9). The two dependencies agree well [34,36,82]. This agreement permits to use the polynomial expression to predict the value of k_c for individual DWNTs for which d_{in}, d_{out}, and then the inter-layer distance, $\delta r = (d_{out} - d_{in})/2$, are known.

It is important to emphasize that this comparison also permits to associate a given value of interlayer distance, δr, to an effective pressure between the layers: an interlayer distance larger or smaller than 0.34 nm leads to an effective negative or positive pressure between the layers [34,84]. Negative (positive) pressure means that the inner-outer interaction causes a slight contraction (expansion) of the outer tube concomitant with the expansion (contraction) of the inner tube. It can be emphasized that the effective pressure (positive or negative) between the tubes reaches gigapascals owing to variations in the wall-to-wall distance [34].

From the knowledge of the dependence of k_c on δr, we can calculate and plot the RBLM frequencies as a function of the diameter of inner (outer) layers for different interlayers distances (Figure 10). As expected, RBLM are upshifted with respect to the RBM of the constituent SWNTs (see also Figure 3b and 3c in [34]), and the RBLM frequencies decrease with increasing diameter of inner (outer) layers. These plots illustrate the strong sensitivity of the RBLM frequencies on the inter-layer distance for the same inner (outer) nanotube diameter. Hence, they are the keys to derive the diameter of the inner and outer tubes of a DWNT from the knowledge of its experimental RBLMs.

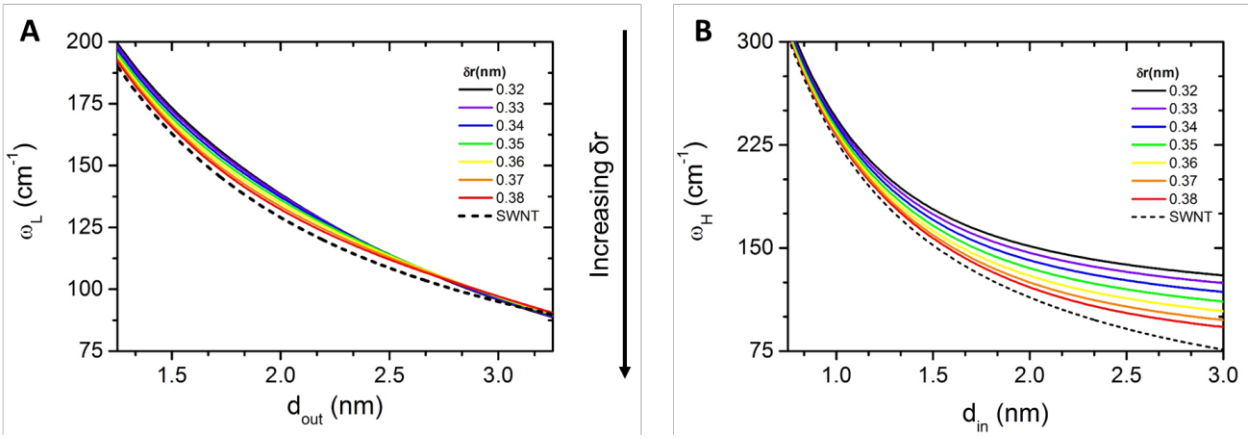

Figure 10: Frequencies of the in-phase (ω_L) and out-of-phase (ω_H) RBLM as function of the diameter of the outer (A) and inner (B) layer for different interlayer distances, δr. In these plots, the following relationships between the RBM frequency and the diameter of inner and outer SWNT are used: $\omega_i = \frac{228}{d_{in}}$ *and* $\omega_0 = \frac{228}{d_{out}}\sqrt{1 + C_e \cdot {d_{out}}^2}$, *with* C_e=0.065 nm^{-2}

4.2.2 The G modes range

Depending on the chiral or achiral character of each constituent SWNT, one expects to observe 4 (chiral@chiral), 3 (chiral@achiral or achiral@chiral) or 2 (achiral@achiral) components in the (// //) polarized Raman spectrum measured on an individual DWNT. However, it must be

emphasized that some components can appear at close frequencies and thus cannot be experimentally resolved. Consequently, the number of observed components can be less than the one predicted for different configurations.

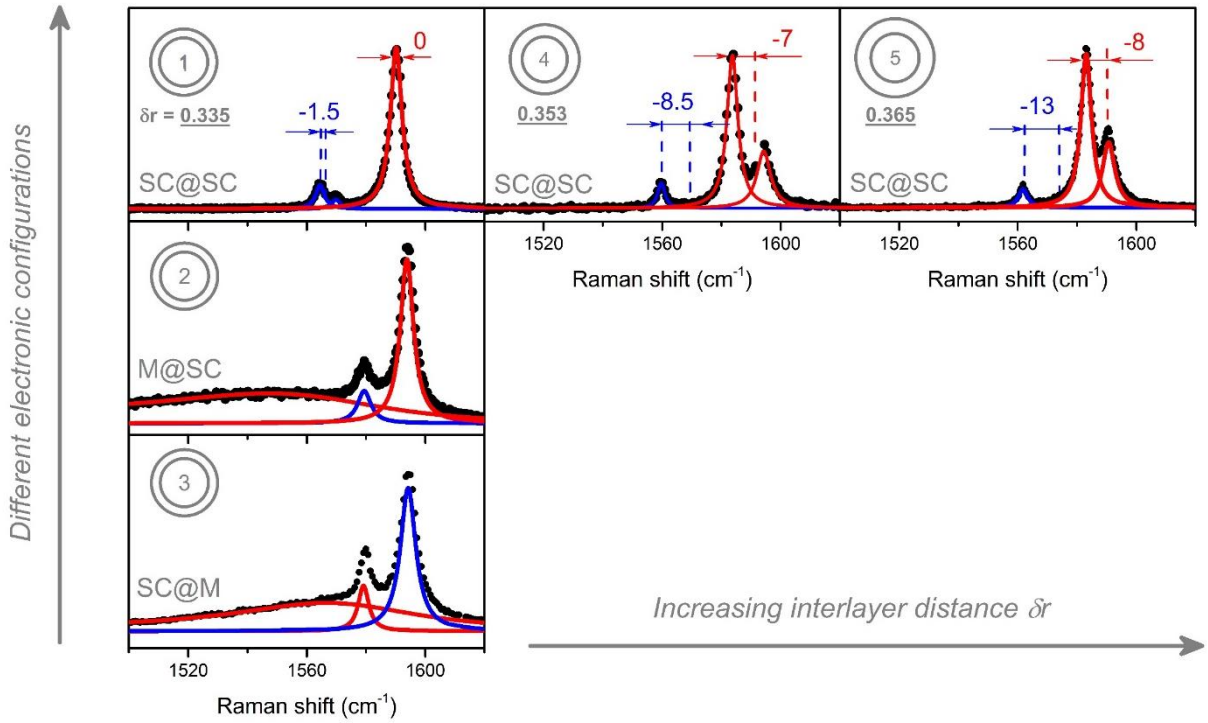

Figure 11: (vertical direction) The dependence of the G modes on the electronic configuration of DWNT: #1 – (12,8)@(16,14) (SC)@(SC), #2 – (14,8)@(19,14) (M)@(SC) , #3 – (14,1)@(15,12) (SC)@(M); (horizontal direction) the dependence of the G modes on the inter-layer distance δr: #4 – (13,9)@(24,7), #5 – (22,11)@(27,17). The shifts of the G modes of the inner tube with respect to the G modes of the related individual SWNTs are given for three semiconducting DWNTs: #1, #4 and #5 (dashed vertical lines).

In Figure 11, we report and compare the profile of G modes measured on index-identified (SC@SC), (M@SC), and (SC@M) DWNTs. By this way, we clearly establish that, as in SWNTs, the profile of G+ or G- component of each layer is broad (narrow) when the layer is metallic (semiconducting). In consequence, the observation of broad component identifies unambiguously the presence of a metallic layer in the DWNT under investigation. This qualitative argument will be used to rule out different possible assignments provided by electron diffraction.

Recently the dependence of the G-modes frequencies on the diameter and inter-layer distance in SC@SC DWNTs was reported [35]. Figure 12 indicates that the TO (G^- component) and LO (G^+ component) frequencies of the inner and outer layer shift significantly in semiconducting DWNTs with respect to the frequencies of the same modes in each constituent SWNT. The direction and values of the shift depend on the inter-layer distance [35]. Especially, as shown in Figures 11 and 12, the shift of the G modes of the inner layer with respect to the G

modes of the related SWNT increases with the inter-layer distance. This shift is due to the negative effective pressure experienced by the inner and outer nanotube which occurs when the inter-layer distance is larger than the equilibrium distance evaluated at 0.335 nm in DWNT (close to the inter-layer distance in graphite, 0.34 nm) [35]. Indeed, the negative pressure is associated with the structural relaxation leading to an expansion of the inner layer. This expansion is the main origin of the softening of the G modes of the inner layers. Consequently, for SC@SC DWNT, the position of the G modes can be used *a posteriori* to confirm the value of the inter-layer distance. Up to now, no equivalent studies concerning the dependence of the G modes for the other electronic configurations of DWNTs have been performed.

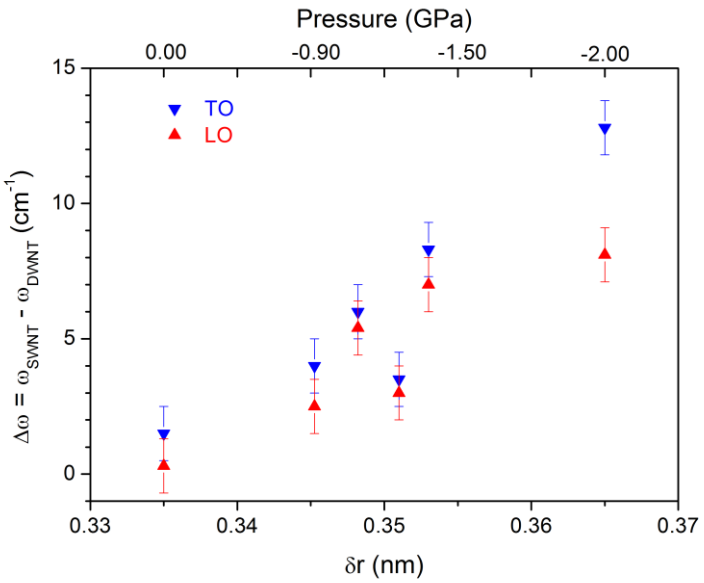

Figure 12: The relationship between G-modes shift and inter-tubes distance established from measurements on index identified SC@SC DWNT (adapted from Ref. [35]*).*

4.2.3 The optical transition energies

The measurement of the complete Raman spectrum of an individual DWNT is only possible when the laser energy E_L is in resonance or quasi-resonance with one of the transition energies, E_{ii}, of inner or outer layers.

Concerning DWNTs, a shift of the transition energies assigned to the inner and outer layers with respect to the corresponding transition energies of the individual constituent SWNT was measured [29]. The magnitude and the direction (up- or downshift) of the shift ranges from -200 meV to +50 meV depending on the chiral structure of the DWNT. Consequently, the best matching of the resonance transitions estimated or measured by Raman spectroscopy on a given DWNT with those expected for the constituent SWNT may provide an additional help to identify

the inner and outer layers. However, the uncertainty of about 100 meV must be accounted for when using a SWNT resonance chart. Finally, similar to SWNTs the other environmental effects like dielectric screening may also shift slightly (tens of meV) the transitions energies in DWNTs.

In summary, the information provided by Raman experiments concerning the frequencies of the radial breathing modes, the line shape and position of the G modes and the transition energies can be used to assign the structure of a carbon nanotube. However, an unambiguous index assignment from Raman data alone should be considered with an extreme care. We show in the next section how the Raman information can be very useful in the DWNT assignment when the electron diffraction fails to identify the structure.

5. Combining electron diffraction and Raman spectroscopy for the index assignment of individual nanotubes

In this part, we discuss the limits of the diffraction methods in some specific situations and we show how the Raman information can help to assign (n,m) indices of the nanotubes. In order to illustrate the application of the EDP treatment methods mentioned in Section 3 we recorded high-resolution transmission electron microscopy images and electron diffraction patterns on 14 individual single-walled and 17 individual double-walled, having different diameters and chiral angles. Multiple EDP and HRTEM images were measured on every individual nanotube. In the following, we focus on the analysis of the ED patterns measured on an individual single-walled and two individual free-standing double-walled carbon nanotubes (see Fig. 13 and Fig. 15).

5.1. Single-Walled Carbon Nanotubes

The EDP recorded on the CNT of the Figure 13, clearly identified as a single-walled carbon nanotube from its HRTEM image (Figure 13, left), is shown on the Figure 13, right. The tube is long and homogenous, which was proved by several measurements of the EDP and HRTEM images in different areas along the nanotube. The following parameters were measured from the diffraction pattern: $\delta = 16 \pm 2$ pixels: $d_1 = (50 \pm 2)$ pixels, $d_2 = (120 \pm 2)$ pixels, $d_3 = (171 \pm 2)$ pixels; for the third layer-line one finds $P_1 = (74 \pm 2)$ pixels, $M_1 = (110 \pm 2)$ and $\Delta_{12} = (25 \pm 2)$ pixels.

Once calibration of the diffraction pattern is established, we get from the first method $\theta = (12.9 \pm 0.2)$ ° and $d = (2.3 \pm 0.5)$ nm. Taking into account uncertainties of d and θ, we are able to propose the following assignments: (i) assuming the tube is semiconducting: (20,6), (23,7), and (29,9), (ii) assuming the tube is metallic: (26,8) and (30,9) SWNTs. Interestingly, following the second method the analysis of the radial oscillations of the third layer lines gives m = 4.

Considering m/n = 0.3213 (from eq. (2)), this leads to n = 12. Thus, the application of the second method gives a (12, 4) SWNT as a possible candidate. This is very far from the five (n,m) indices established by the first approach. The reason for this discrepancy is related to the high-sensitivity of the layer-line intensity distribution to the tilt of the nanotube. Finally, the estimation of the (n, m) from the intrinsic layer lines (method 3) gives n = 25.22 and m = 7.7. If we don't consider the tilt-effect, we get (25,7) SWNT. However, by measuring the tilt angle, we find $\tau = 25°$ and the tilt-corrected (n,m) value is (23,7).

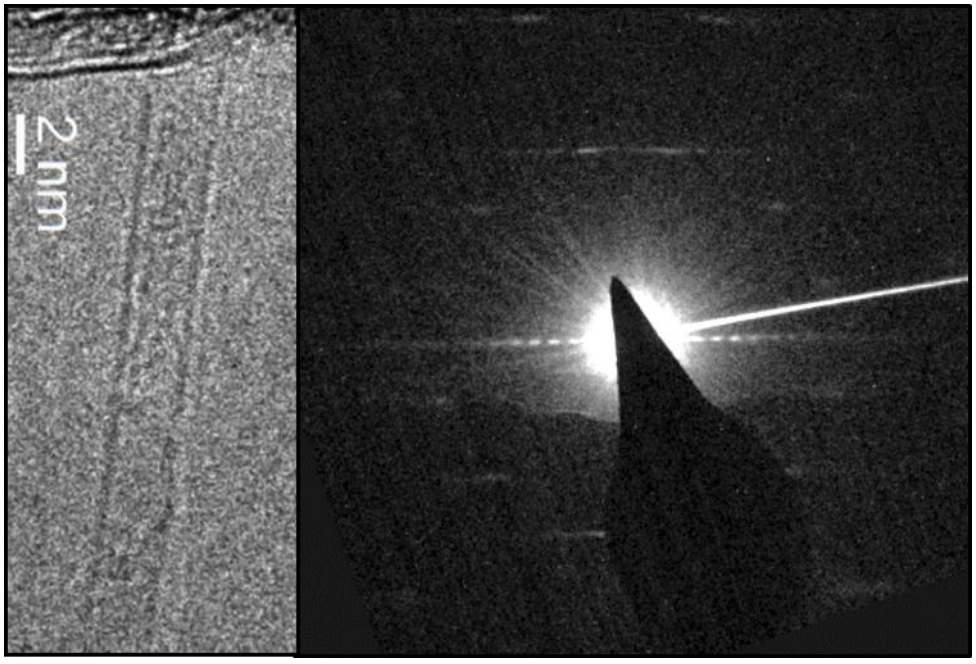

Figure 13. HRTEM micrograph (left) and electron diffraction pattern (right) of a chiral single-walled carbon nanotubes, analyzed in this work.

As indicated in table 2, the analysis of the ED pattern of this specific SWNT performed by using three different methods, is only able to propose four possible assignments, namely: (12, 4), (20,6), (23,7), and (29,9) if this tube is semiconducting, and 2 possible assignments, namely: (26,8) and (30,9), if the tube is metallic. However, it must be pointed out that the (23,7) assignment is the only one that is derived from two distinct methods.

	Method 1		**Method 2**		**Method 3**	
	Exp. values	#	Exp.values	#	Exp. values	#
1	$d = (2.3 \pm 0.5)$ nm $\theta = (12.9 \pm 0.2)°$	5	$(m/n)_i = 0.3213 \pm$ $n_{in} = 4$	1	$n_i = 25.22 \pm$ $m_i = 7.70 \pm$	1

Table 2. The possible assignments of a SWNT derived from the electron diffraction. The number # of possible indices found by the different methods is indicated (see text for details).

Raman measurements were performed at different excitation energies and the corresponding spectra close to the incident resonances, namely E_L=1.66 eV, 2.21 eV and 2.71 eV and close to the outgoing resonance for the G-modes, E_L=1.83 eV, are shown on Figure 14. Concerning the structure of the SWNT under investigation, the information states by Raman are: (i) From the RBM frequency, located at 128.5 ± 3 cm^{-1}, its diameter is estimated as 2.01 ± 0.06 nm by applying the relation (6) and using C_e=0.065 nm^{-2}. Obviously, this diameter is in the range suggested by ED (except for method 2). (ii) From the G-band profile, we can infer that this single-walled nanotube is semiconducting and chiral. (iii) From the Raman resonance conditions, transition energies close to 1.66 eV, 2.21 eV and 2.71 eV are identified.

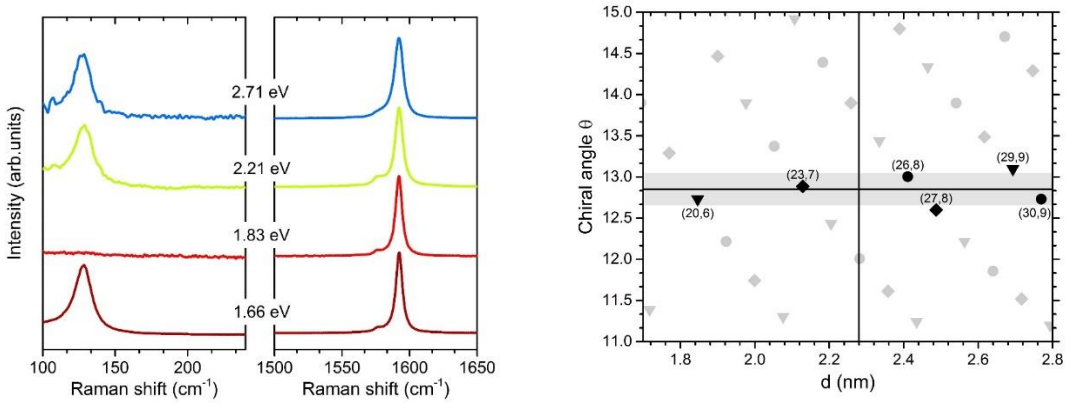

Fig. 14. (left) RBLM part and G-mode part of the Raman spectra of an individual SWNT measured at different excitation wavelengths: 457 nm (2.7eV), 561 nm (2.21 eV), 679 nm (1.83 eV) and 745 nm (1.66 eV); (right) Index-assignments of the possible semiconducting SWNT located in the diameter range 1.7-2.8 nm. The grey area represents the chiral angle range derived from the analysis of the electron diffraction pattern of the SWNT under investigation. Vertical line indicates the diameter measured from EDP. Triangle and diamond symbols represent SC SWNTs and solid dots M SWNTs.

In order to assign the (n,m) indices of this tube, we gather the TEM-ED and Raman information on the graph of the Figure 14 (right). On this graph, the chiral angle is set from the value measured by electron diffraction with an error bar of ± 0.2° and corresponds to the grey area. The vertical line indicates the average diameter of nanotube derived from electron diffraction. Due to the poor accuracy in the evaluation of diameter by ED, we consider a broad range of error bar, ± 0.5 nm.

Among all the possible semiconducting candidates, the RBM frequency and the theoretical value of the chiral angle of only one semiconducting SWNT, namely the (23,7), are in the closest agreement with the RBM frequency measured by Raman and with the chiral angle derived from

EDP. In addition, the comparison of three experimental transition energies with those calculated/measured in Ref. [21,79] are only in good agreement for the (23,7) SWNT and fails for the other possible candidates. Consequently, we conclude that the most probable assignment for this single-walled nanotube is (23,7). It must be emphasized that this assignment corresponds perfectly with the results made by the third method of EDP treatment.

Transition energies of the (23, 7) SWNT	Experimental resonance energies	Ref. [38,65]	Ref. [21]
E_{33} (eV)	1.66 eV	1.72	1.69
E_{44} (eV)	2.21 eV	2.21	2.23
E_{55} (eV)	2.71 eV	2.58	2.57

Table 3. Experimental and calculated optical transition energies E_{ii}.

5.2. Double-Walled Carbon Nanotube

Figure 15A shows the EDP and HRTEM image of a long CNT, clearly identified as a double-walled carbon nanotube (DWNT1) from the HRTEM image (Figure 15A, left). Due to its high quality, the analysis of the HRTEM image permits to evaluate with a good accuracy the diameter of each layer: $d_{out} = 3.2 \pm 0.3$ nm and $d_{in} = 2.5 \pm 0.3$ nm.

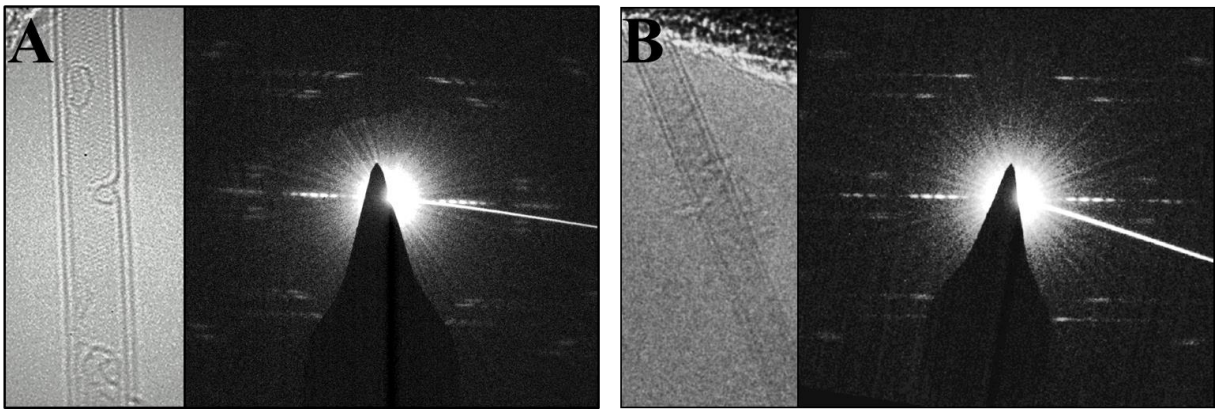

Figure 15. HRTEM micrographs and electron diffraction pattern of two chiral double-walled carbon nanotubes, analyzed in this work. (A) DWNT 1 and (B) DWNT 2 (see text)

We now follow the procedure established in the Section 3 and report all the possible information from the EDP. First, the principle layer-lines are grouped in two sets according to the zone method and conjugation principle: $d_1^A = (42.0 \pm 0.7)$ pixels, $d_2^A = (168.0 \pm 0.7)$ pixels, $d_3^A =$

(210.0 ± 1.4) pixels and d_1^B = (28.3 ± 0.7) pixels, d_2^B = (176.2 ± 0.7) pixels, d_3^B = (206.0 ± 1.4) pixels. By comparing relative intensities of L_3^A and L_3^B , and L_2^A and L_2^B layer lines, we find that set B correspond to the outer layer, while set A to the inner. From the equatorial line oscillations of the EDP we find E = (126 ± 2.0) pixels and e = (17.25 ± 0.35) pixels. Finally, since the signal-to-noise ratio is sufficiently high for the EDP of this DWNT, we are able to measure the peak separation of principle layer-lines in the radial direction. The intensity distribution of the L_3^A layer-line gives P_1^A = (148 ± 2) pixels, P_2^A = (218 ± 2) pixels, M_1^A = (189 ± 2) pixels, Δ_{12} = (27 ± 2) pixels. Consequently, the following ratios were established: $R_1 = P_2^A/P_1^A$ = 1.473 ± 0.026; $R_2 = P_1^A/\Delta_{12}$ = 5.481 ± 0.438; $R_3 = M_1^A/\Delta_{12}$ = 7 ± 0.556. The intensity distribution of the L_2^A layer-line gives R_1 = 1.253 ± 0.011; P_1^A/Δ_{12} and M_1^A/Δ_{12} are not established due to the unresolved Δ_{12}. Finally, the intensity distribution of the L_3^B layer-line provides R_1 = 1.310 ± 0.020, R_2 = 7.652 ± 0.712 ; R_3 = 9.087 ± 0.843. And for L_2^B one has R_1 = 1.240 ± 0.012. Again, R_2 and R_3 in this case are not established due to the unresolved Δ_{12}. All the uncertainties were calculated using the principle of error propagation.

We now apply three distinct methods, mentioned above, and find all the possible (n,m) candidates for this DWNT. Following Method 1, we find <d>= 3.0 ± 0.4 nm and δr = 0.42 ± 0.05 nm (see expression 4) or equivalently d_{out}= 3.4 ± 0.4 nm and d_{in}= 2.6 ± 0.4 nm. The two chiral angles were established from relation (1): θ_{out} = 22.4 ± 0.4° and θ_{in} = 19.1° ± 0.4°. Combining diameter and chiral angle values for two constituent layers and taking into account the corresponding uncertainties, we obtain the following combinations: (22,11)@(27,17), (26,13)@(30,19) if both layers are semiconducting, and (24,12)@(29,18), (26,13)@(31,19), (28,14)@(32,20) if one of the layers is metallic. Overall, Method 1 provides five distinct combinations (see Table 3).

From the comparison between theoretical and experimental R_1, R_2 and R_3 following Method 2, one finds for L_3^A layer line m = 8 (on the basis of R_1), m = 8 and 9 (R_2), m = 9 and 10 (R_3). The L_2^A layer-line gives n = 19, 20 (R_1). We then calculate all possible combinations of n, m: (20,8), (19,8), (19,9), (20,9), (20,10) and (19,10). However, if we compare m/n for each of this combinations with the experimental value of $(m/n)_A = 0.500 \pm 0.013$ (eq. (2)), we find, that only CNT (20,10) with m/n = 0.500 is compatible. The second set of layer lines provides the following indices for the outer layer: m = 13, 14, 15 (R_1), m = 13, 14, 15, 16 (R_2), m = 13, 14, 15, 16 (R_3); n = 20, 21, 22 (R_1). Keeping in mind the experimental $(m/n)_B = 0.624 \pm 0.016$ only (22,14) with 0.6364 and (21,13) with 0.6190 are possible. Consequently, the application of the second method gives (20,10)@(22,14) and (20,10)@(21,13) as possible candidates. However,

these candidates are completely unrealistic due to the very small interlayer distance: δr = 0.195 nm and 0.128 nm, respectively. The problem with this index assignment can be due to the following reason: layer-line intensity distribution is very sensitive to the tilt of the nanotube to the incident beam. As was shown by Jiang et al. [51], at high tilt-angles the method of Bessel function analysis fails completely.

At last, using the third method we can estimate n and m directly from the "intrinsic layer lines" by equations (5): $n_i = 22.862 \pm 0.607$ and $m_i = 11.431 \pm 0.328$; $n_o = 28.159 \pm 0.618$, $m_o = 17.577 \pm 0.399$. First, if we don't consider the effect of the tilt, we get (22,11)@(28,17) or (23,11)@(28,17) as the indices of the DWNT. However, by accounting for the non-zero tilt, we can find following combinations: (22,11)@(27,17) with $\tau \approx 16°$; (20,10)@(25,15) with $\tau \approx 29°$ and (18,9)@(23,14) with $\tau \approx 38°$. The last one can be discarded due to unreasonably high tilt. Hence, the tilt-corrected combinations are (22,11)@(27,17) and (20,10)@(25,15). In summary, the analysis of the ED pattern of this specific DWNT performed by three different methods, allows us to propose eight possible distinct candidates (Table 4).

The ED pattern of the second double-walled carbon nanotube (DWNT 2) is shown in the Fig. 15B (right). The tube is long and homogenous, which was proved by several measurements of the EDP and HRTEM images in different areas along the nanotube. It should be noted, that the layers of this DWNT have close chiral angles, so the analysis of the radial intensity distribution using Method 2 is not possible. The results of the index-assignment are summarized in Table 4.

	Method 1		**Method 2**		**Method 3**	
	Exp. values	#	Exp.values	#	Exp. values	#
DWNT 1	d_{in} = (2.6 ± 0.4) nm d_{out} = (3.4 ± 0.4) nm θ_{in} = (19.1 ± 0.4)° θ_{out} = (22.4 ± 0.4)°	5	$(m/n)_{in} = 0.500 \pm 0.013$ $(m/n)_{out} = 0.624 \pm 0.016$ n_{in}=8-10 m_{in}=19-20 n_{out}= 20-22 m_{out}=13-15	2	$n_i = 22.862 \pm 0.607$ $m_i = 11.431 \pm 0.328$ $n_o = 28.159 \pm 0.618$ $m_o = 17.577 \pm 0.399$	2
DWNT 2	d_{in} = (2.17 ± 0.66) nm d_{out} = (2.97 ± 0.66) nm θ = (21.14 ± 0.83)°	13	m/n = 0.380 ± 0.023 Layer-lines overlapped (Method not applicable)	-	$n_i = 14.366 \pm 2.296$ $m_i = 5.456 \pm 0.901$ $n_o = 23.043 \pm 2.316$ $m_o = 8.752 \pm 0.952$	2

Table 4. The results of EDP analysis of DWNT 1 and DWNT 2 (see text).

It is clear that electron diffraction does not permit to determine unambiguously the index-assignment of the layers of these two DWNTs. As expected, Raman information permits to exclude some of the possible candidates.

DWNT 1: The RBLM part and G-mode part of the Raman spectra measured at different excitation energies, are displayed in Figure 16.

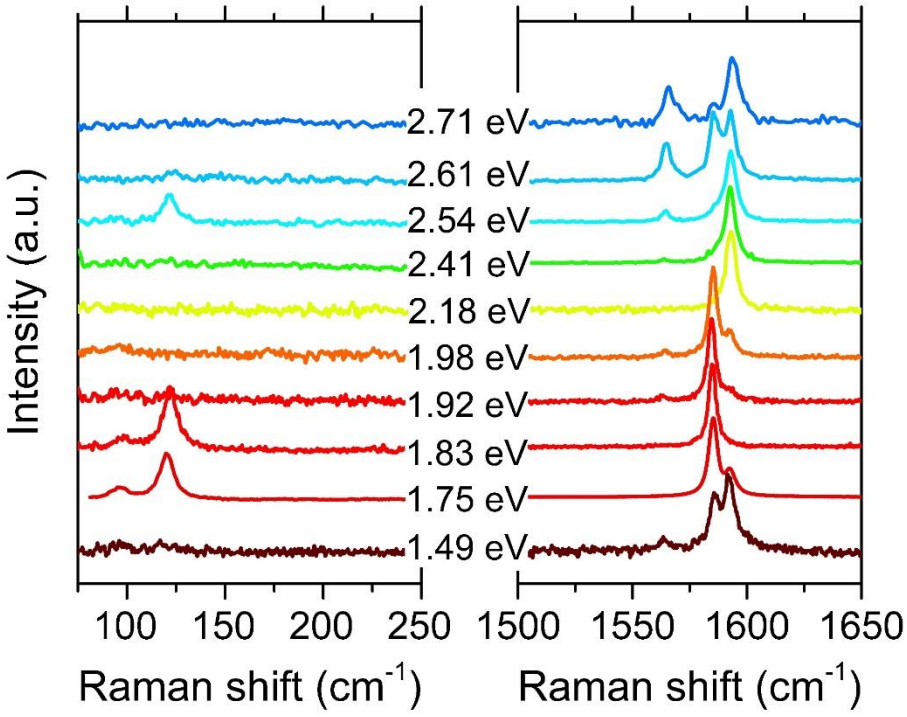

Figure 16: DWNT 1: The RBLM part and G-mode part of the Raman spectra measured at different excitation energies.

The in-phase and out-of-phase modes are located at 98 ± 3 cm^{-1} and 121 ± 3 cm^{-1}, respectively. By using modelisation detailed in Section 4.2.1, we plot in the Figure 17 the calculated iso-frequency curves corresponding to the experimental ω_L (98 ± 3 cm^{-1}) and ω_H (121 ± 3 cm^{-1}) RBLMs as a function of nanotube diameter and inter-wall distances. From these curves, we can estimate the diameters of the inner and outer tubes at 2.24 ±0.1 nm and 2.96 ±0.1 nm, respectively. As expected, both diameters are in the range predicted by electron diffraction. The average inter layer distance is estimated close to 0.36 nm with an error bar of ±0.03 nm. It must be emphasized the error bars of diameters and interlayer distance are smaller that the ones derived from ED. This later point emphasizes the efficiency of the Raman spectroscopy, associated to a modelisation of the RBLM frequencies, to derive information on diameters and interlayer distance in DWNT.

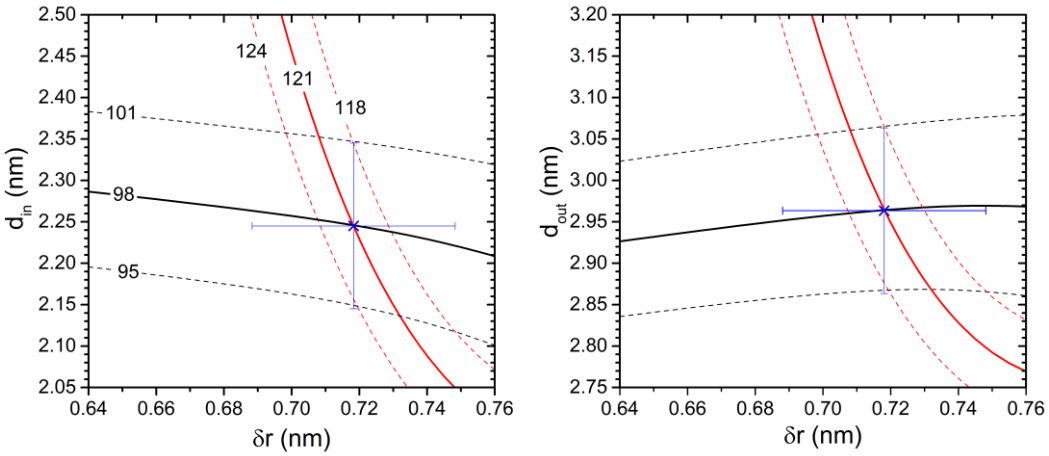

Figure 17: Iso-frequencies RBLM curves as a function of the diameter of inner (left) or outer (right) layer and interlayer distance δr.

On the other hand, the absence of broad components in the G-band indicates that both layers of the DWNT under consideration have a semiconducting character. Finally, by analyzing incident and outgoing resonance conditions (see Figure 16) and two additional resonant Raman excitation profiles (measured between 1.92 - 2.18 eV and 1.50 – 1.75 eV, not shown in Fig. 16) of RBLMs and G-band, we estimated the values of transition energies to be at 2.54, 2.03, ~ 1.80 and 1.60 eV.

In order to determine the $(n_i,m_i)@(n_o,m_o)$ indexes of this DWNT, we plot the ED and Raman-derived information on the Figure 18. In particular, blue and red horizontal lines correspond to the two average chiral angles obtained from the electron diffraction (uncertainly of 0.2°). The inner (bottom) and outer (top) diameter scales are centered around the average diameter values derived from ED and HRTEM. Additionally, they are aligned to have an interlayer distance of 0.36 nm, which was previously established from iso-frequency curves. Finally, the solid symbols indicate all possible $(n_i,m_i)@(n_o,m_o)$ obtained from electron diffraction: circles correspond to the metallic layers, while triangles and diamonds to the semiconducting ones. In order to take into account the error of 0.03 nm on the interlayer difference derived by Raman, the error bar is applied to the diameter of the outer tube.

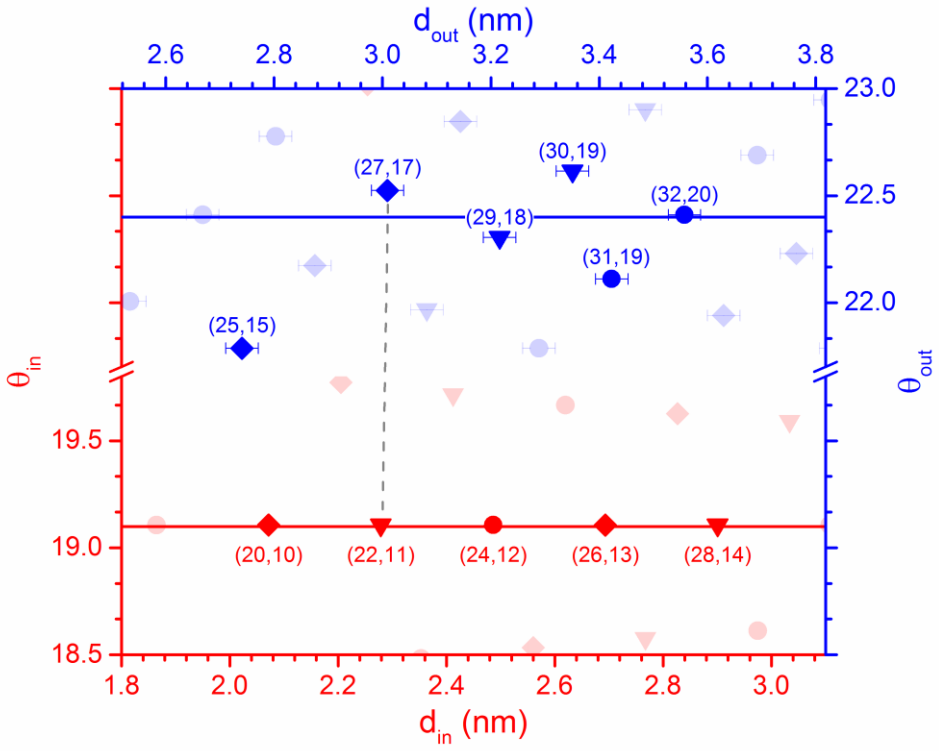

Figure 18: (a) Possible inner and outer layers constituting DWNT 1 from its EDP analysis.

To determine the possible assignments, we consider all SC@SC DWNT which have diameters in the ranges derived from ED and Raman. The possible assignments can be visually determined by looking for a couple of (n,m) (one in the bottom and one in the top part of the graph) which are vertically aligned and falls within the ±0.03 nm error bar range of the interlayer distance. For the DWNT under investigation, only the (22,11)@(27,17) is compatible with all the previous criteria. Notice that electron diffraction proposes two (out of total five) possible semiconducting assignments, namely: (22,11)@(27,17), (26,13)@(30,19). Obviously, the assignment provided by taking into account the Raman information is one of those predicted from electron diffraction.

DWNT 2: The assignment of the second DWNT (DWNT 2) is detailed below. In the Figure 15B, we show the high-resolution and the EDP of the nanotube. The analysis of the EDP provides following values for the chiral angles: 20.3 ± 0.2° and 21.6 ± 0.2°. From the TEM image and the EDP the diameters of inner and outer tubes are estimated as 1.65 ± 0.5 nm and 2.3 ± 0.5 nm, respectively.

Raman measurements were performed at different excitation wavelengths and representative spectra are shown in Figure 19. From the G-bands line-shape at 2.71 eV and 2.41 eV, we can infer that the inner (outer) layer of this DWNT is chiral metallic (chiral semiconducting). The in-phase and out-of-phase RBLM are observed at 120 cm^{-1} and 157 cm^{-1},

respectively. Using the previously presented procedure, we can derive: i) the diameters of the inner and outer layers which are, respectively, 1.7±0.1 nm and 2.4±0.1 nm and ii) the inter-layer distance: 0.34±0.03 nm.

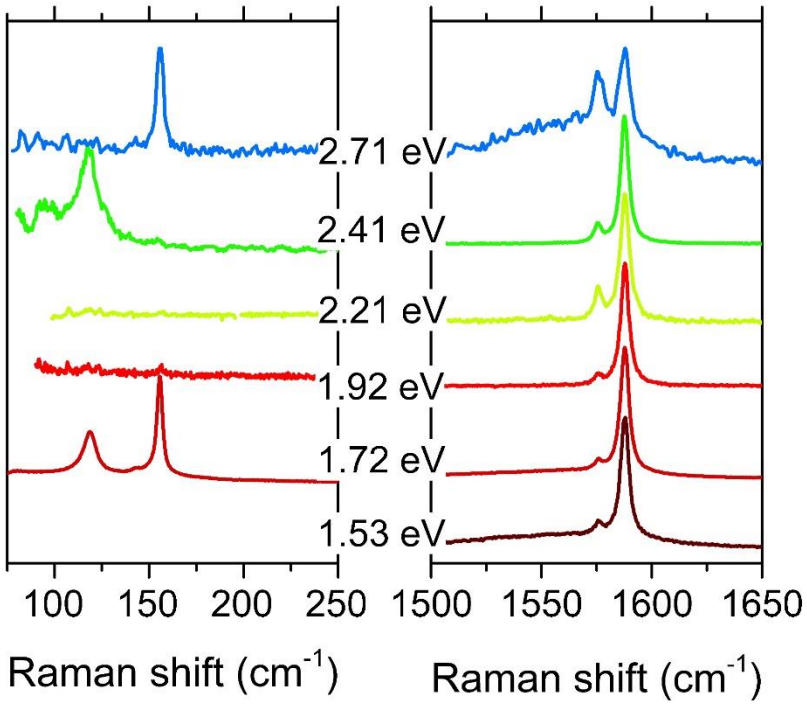

Figure 19. DWNT 2: The RBLM part and G-modes part of Raman spectra measured at different excitation energies.

By considering all the possibilities of $(n_i,m_i)@(n_o,m_o)$ reported on Figure 20, we propose to assign this DWNT as (15,9)@(22,12). The theoretical values of the diameters and interlayer distance of the (15,9)@(22,12) DWNT are in good agreement with those derived from the analysis of the Raman and ED data.

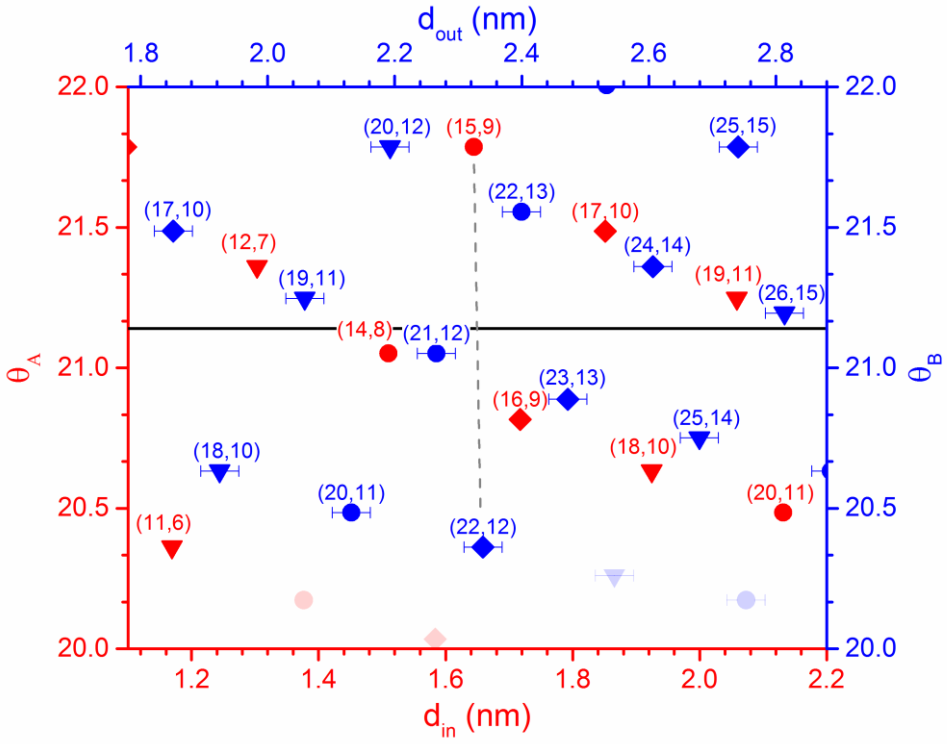

Figure 20. Plot of the chiral angles as function of diameters for inner (bottom-left scale) and outer layers (top-right scale) for DWNT 2. The horizontal black line represents the same chiral angles of both inner and outer layers as identified from electron diffraction (see text).

6. Beyond SWNTs and DWNTs.

A triple-walled carbon nanotube (TWNT) is a coaxial composite of three SWNTs which interact with each other by weak van der Waals forces. A HRTEM image of an individual free-standing TWNT is shown on the Figure 21. The TWNT is fully defined by chiral indices (n_i, m_i)@(n_{int},m_{int})@ (n_o,m_o) of each coaxial layer (inner, intermediate and outer layers respectively). Depending on the semiconducting or metallic character of each layer, TWNT present eight different electronic configurations, namely: SC@SC@SC, SC@SC@M SC@M@SC, M@SC@SC, M@M@SC, SC@M@M, M@SC@M and M@M@M.

From a fundamental point of view, the interest to study individual free-standing TWNTs is multiple: (i) Determination of their intrinsic properties, including optical and vibrational properties, (ii) Investigation of the intrinsic inter-tube interactions occurring in DWNT since the outer concentric nanotube shields the two inner nanotubes from external environmental influences, (iii) Unrolled TWNT can be view as a triple layer graphene ribbon, a material with outstanding properties.

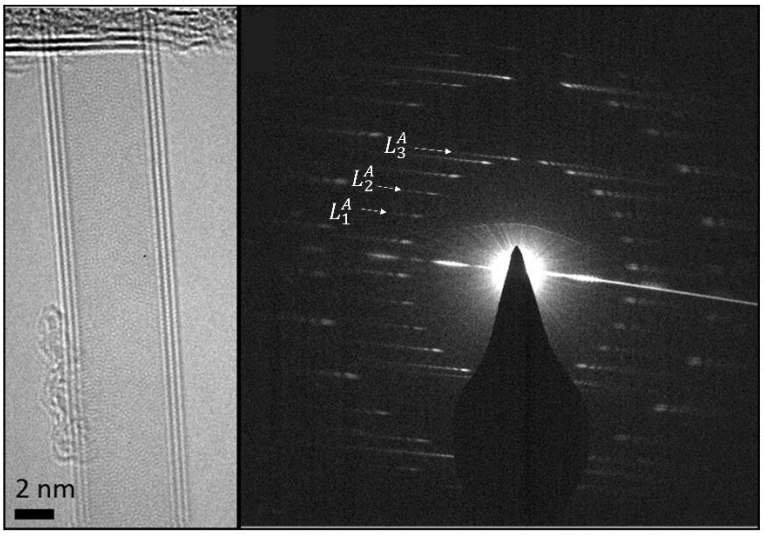

Figure 21: The HRTEM image (left) and electron diffraction pattern (right) of the triple-walled carbon nanotube investigated by combining ED and Raman spectroscopy. Labels L_1^A, L_2^A and L_3^A indicate layer-lines, that correspond to $\theta = 7.2°$ (see text for details).

In principle, the chiral indices of each layer of a TWNT, (n_i, m_i),(n_{int}, m_{int}) and (n_o, m_o) respectively, can be derived from the analysis of its diffraction pattern (Figure 21, right). The analysis of the EDP is similar to the double-walled case (see Section 3 for details), except one needs to consider the third set of layer-lines. The main difficulty arises from the analysis of the equatorial line, which cannot be described by a simple analytical relationship suitable for the extraction of the diameters of the constituent layers. In this case, one needs to provide a high quality HRTEM image to roughly estimate the layers' diameters.

Similar to DWNTs, the Raman information can greatly contribute to the structure identification of TWNTs. However, up to now, no investigation of index identified TWNTs has been performed by Raman spectroscopy, and, in consequence, only qualitative Raman arguments can be given to help at the index-assignment of TWNTs. Raman spectra of TWNTs have been recorded only on bundles of TWNTs and on few individual TWNTs deposited on a silicon substrate (see for instance, the Ref. [85]). The individual TWNT investigated in Ref. [85] were prepared through high-temperature treatments of the peapods fullerenes inside of diameter-enlarged CVD grown DWNT. This method is known to provide inner nanotubes with diameter close to 0.7 nm [86]. These studies mainly focus on the dependence of the innermost tube RBM on its metallic or semiconducting character. In particular, the metallic innermost tube is considered to be more isolated from the intermediate layer since its RBLM frequencies are located closer to the position of the RBM in the corresponding metallic SWNTs. On the other hand, the peaks of

semiconducting innermost tubes are always upshifted with respect to the RBMs in the corresponding semiconducting SWNTs.

To illustrate the route for the indexation of individual TWNTs, we report and discuss the combined electron diffraction and Raman data recorded on the individual free-standing TWNT of the Figure 21.

6.1 HRTEM and electron diffraction

The high quality of the HRTEM image of the individual free standing TWNT allows us to evaluate with a relatively good accuracy (± 0.5 nm) the diameter of each layer. We found d_{in} = 4.5 nm, d_{int} = 5.2 nm and d_{out} = 5.8 nm. From the quick glance at the EDP (Fig. 21 right) one can find 6 layer-lines instead of 9, which indicates that two layers of the TWNT have the same chirality. The EDP treatment, following the procedure established in Section 3, gives the following chiral angles: 7.2 ± 0.3° and 21.5 ± 0.3°. The comparison of the relative intensities of the layer-lines clearly showed that 7.2° correspond to the single layer, while the other two layers have 21.5°. Additionally, analyzing radial oscillations of the L_3 layer line (shown as L_3^A in Figure 21) , it was found that the single layer should have m = 7 or 8. Given m/n = 0.158 ± 0.006, we find 8 possible candidates for this layer: 5 semiconducting, namely: (44,7), (45,7), (49,8), (51,8), (52,8), and 3 metallic, namely: (43,7), (46,7), (50,8). The diameters of these candidates are closer to d_{in} = 4.5 nm than to d_{int} and d_{out}, established from HRTEM, which indicates that the single-chirality layer is the inner one. Finally, the (n,m) indices of the intermediate and outer layers were established by searching candidates with the following parameters: m/n = 0.588 ± 0.01, d_{int} = 5.2 ± 0.5 nm and d_o = 5.8 ± 0.5 nm. 7 intermediate (n,m) indices: (50,29), (48,28), (46,27), (51,30), (44,26), (49,29), (47,28), and 8 outer indices: (57,33), (55,32), (53,31), (58,34), (56,33), (54,32), (52,31), (57,34) were found. From all these candidates 5 TWNT combinations can be proposed, if we assume interlayer distance to be δr > 0.32 nm: (50,8)@(46,27)@(52,31), (50,8)@(46,27)@(53,31), (51,8)@(46,27)@(52,31), (51,8)@(46,27)@(53,31), (52,8)@(47,28)@(54,32). The first three combinations have metallic layers, while the other two are purely semiconducting.

6.2 Resonant Raman spectroscopy

The Raman spectra of this individual free-standing TWNT were measured in a wide range of laser excitation energies (1.83 eV-2.71 eV). The spectra with the best signal to noise ratio have been measured at 2.41 eV and 2.18 eV and they are displayed in Figure 22.

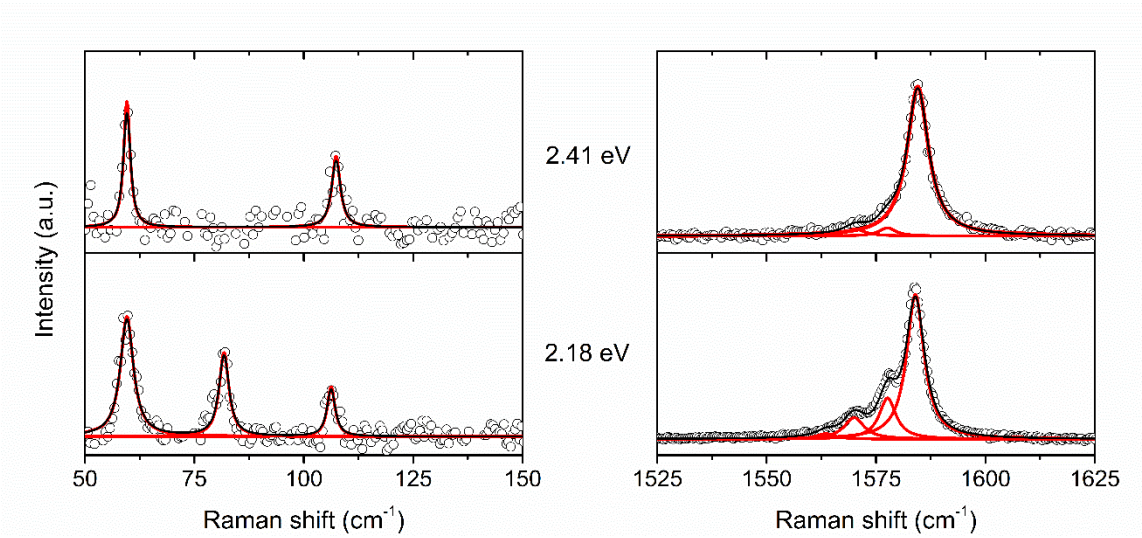

Figure 22. Raman spectra measured at 2.41 eV (top) and 2.18 eV (bottom) on the individual TWNT identified by HRTEM and ED (see Figure 21).

We first analyze the information provided by the features of the G modes (Figure 22, right). In agreement with the behavior established from experiments performed on index-identified DWNTs, the absence of a broad component in the G modes part of the Raman spectra recorded for a broad excitation range states that all the layers of the TWNT under investigation have a semiconducting character. Then, the seven configurations, in which at least one metallic layer is present (namely, M@SC@SC, SC@M@SC, M@M@SC, etc…), are ruled out, and the single remaining configuration for the TWNT under consideration is: SC@SC@SC.

G modes are located at 1570, 1578, 1584 cm^{-1} and well fitted by considering a Lorentzian profile for each component, in agreement with the semiconducting character of each constituent layer. The relative intensities of the three components show a dependence on the excitation energy. On the basis of the behavior established for SWNTs [65] and with regards to the large diameters of the layers of the investigated TWNT, we can expect: (i) a close values (overlap) of the TO and LO mode of each layer, and (ii) a highest-frequency of the G mode close to the one measured in trilayer graphene. The presence of a highest-frequency G mode located at 1584 cm^{-1} is in agreement with this assumption. It can be also noted that such a low frequency of the G+ component was also reported in Ref. [87]. By analogy with the behavior found for the G modes of the inner layers in DWNT, the two other peaks at 1578 and 1570 cm^{-1} can be tentatively assigned to the TO-LO modes of the intermediate and inner layers respectively. As for the G modes of the inner layer in DWNT, the downshift of these both TO-LO G modes can be assigned to the effective pressure experienced by the intermediate and inner layers in TWNT.

The RBLM part of Raman spectra (Figure 22 left) excited at 2.18 eV show three RBLMs, as expected for an individual TWNT [88]. These peaks are located at 60, 84 and 107 cm^{-1} respectively. All the RBLM lines have a very low-intensity certainly due to the large diameter of the constituent layers. Only the lowest- and highest-frequency RBLMs appear in the spectrum excited at 2.41 eV.

As for DWNT, only the optical resonance of one layer is necessary to observe the response of a coupled system such as a TWNT [31,34]. Then, the presence of one, two or three RBLMs at a given excitation energy means that at least one constituent layer is in close resonance at this excitation energy. From the spectra of the Figure 22, for the TWNT under investigation we predict optical transitions, E_{ii}, of constituent layers close to 2.41 eV and 2.18 eV. Resonance excitation profile (not shown) measured between 2.00 - 2.17 eV excitation range suggests another transition around 2.03 eV. At this stage, it is impossible to assign precisely a transition to a specific layer.

The RBLM frequencies are very different to those predicted for the constituent layers. Indeed, the RBM frequencies for SWNTs of diameters $d_o = 5.8$ nm, $d_{int} = 5.2$ nm and $d_i = 4.5$ nm are expected close to 39, 44 and 51 cm^{-1} in strong disagreement with the experimental ones. The strong difference between the RBLMs and the corresponding RBM is amplified due to the large diameters of the layers in the TWNT under investigation.

In TWNTs, the RBLM frequencies depend on the diameter of the layers and on the distances between two consecutive layers. Both distances, namely: outer-intermediate layer and intermediate-inner layer, define the van der Waals interactions and mechanical coupling between the layers. Taking into account the van der Waals interactions, V. N. Popov and L. Henrard have calculated the features of the RBLMs of TWNTs with layers of armchair type and outer diameters ranging from 2 to 3.6 nm [88]. These calculations show that for small diameter TWNT, such as (5,5)@(10,10)@(15,15), the displacement pattern of each RBLM is characterized by motion of atoms of mainly one layer. For large diameter TWNT such as (15,15)@(20,20)@(25,25), the RBLMs are collective motions of all three layers. In this later situation, which corresponds to the one of the TWNT under consideration (large diameter of the constituent layers), the lowest-frequency RBLM is an in-phase mode and the two other higher-frequency RBLM are of mixed character. The dependence of the frequencies of three RBLMs on the outer layer diameter ranging from 2 to 3.6 nm is shown in the Figure 5 of the Ref. [88]. The extrapolation of these calculations to the diameter of the outer layer close to 5.8 nm predicts the lowest-frequency RBLM at 47 cm^{-1}, downshifted by 13 cm^{-1} with respect to the experimental frequency (60 cm^{-1}). The relatively poor agreement between experiment and calculation means that more sophisticated models have to be

developed. These models will have to take into account explicitly the effects of two different interlayer distances on the RBLM frequencies.

By combining ED and available Raman information, in particular the semiconducting character of the layers, we can reduce the number of possible candidates for the TWNT under consideration to two combinations: (51,8)@(46,27)@(53,31) or (52,8)@(47,28)@(54,32).

7. Conclusions and Perspectives

In this paper we reviewed the main results obtained by combining high-resolution transmission electron microscopy (HRTEM), electron diffraction (ED) and resonant Raman spectroscopy (RRS) measurements on individual free-standing single-walled (SWNT) and double-walled carbon nanotube (DWNT). A special attention was focused on double-walled carbon nanotubes (DWNT).

As reported and discussed in a first part of this paper, HRTEM and ED are the most powerful methods for the structure analysis at the single nanotube level. Well established Raman results obtained on SWNTs and DWNTs, unambiguously identified by HRTEM and ED, were reported. Especially, the dependencies of the main features of the phonons (profile, frequency, resonance conditions) of individual free standing SWNTs and DWNTs as a function of their structural parameters were shown and discussed.

In the second part, we demonstrated that, in some specific situations, electron diffraction fails to identify the structure of individual nanotubes. In such situations, we highlighted that the combination of HRTEM, ED, and RRS permits to suggest the most accurate index-assignment of individual SWNTs and DWNTs. Such experimental coupling is particularly relevant for studying complex carbon nanostructures such as TWNTs.

Acknowledgments

D. L. gratefully acknowledges financial support of Russian Science Foundation (grant number 15-12-10004). NT, MP, TM, AAZ, and JLS acknowledge financial support by the ANR GAMBIT project, grant ANR-13-BS10-0014 of the French Agence Nationale de la Recherche and the International project of Scientific Cooperation with Vietnam (CNRS PICS 6457). The TEM studies were conducted at the Laboratorio de Microscopias Avanzadas, Instituto de Nanociencia de Aragon, Universidad de Zaragoza, Spain. Some of the research leading to these results has received funding from the European Union Seventh Framework Program under Grant Agreement 312483 ESTEEM2 (Integrated Infrastructure Initiative – I3) and from the European Union H2020

program under the grant 696656 Graphene Flagship. R.A. gratefully acknowledges the support from the Spanish Ministry of Economy and Competitiveness (MINECO) through project grant FIS2013-46159-C3-3-P, from the Government of Aragon and the European Social Fund under the project “Construyendo Europa desde Aragon” 2014-2020 (grant number E/26), and from the European Union H2020 program under the ETN project “Enabling Excellence” Grant Agreement 642742.

References

[1] M.F.L. De Volder, S.H. Tawfick, R.H. Baughman, A.J. Hart, Carbon Nanotubes: Present and Future Commercial Applications, Science. 339 (2013) 535–539. doi:10.1126/science.1222453.

[2] S. Reich, C. Thomsen, J. Maultzsch, Carbon Nanotubes: Basic Concepts and Physical Properties, 1st ed., WILEY-VCH Verlag GmbH & Co. KGaA, 2004.

[3] N. Tanaka, J. Yamasaki, T. Kawai, H. Pan, The first observation of carbon nanotubes by spherical aberration corrected high-resolution transmission electron microscopy, Nanotechnology. 15 (2004) 1779–1784. doi:10.1088/0957-4484/15/12/015.

[4] A. Hashimoto, K. Suenaga, K. Urita, T. Shimada, T. Sugai, S. Bandow, H. Shinohara, S. Iijima, Atomic correlation between adjacent graphene layers in double-wall carbon nanotubes, Phys. Rev. Lett. 94 (2005) 1–4. doi:10.1103/PhysRevLett.94.045504.

[5] H. Zhu, K. Suenaga, J. Wei, K. Wang, D. Wu, Atom-resolved imaging of carbon hexagons of carbon nanotubes, J. Phys. Chem. C. 112 (2008) 11098–11101. doi:10.1021/jp804385a.

[6] C.S. Allen, A.W. Robertson, A.I. Kirkland, J.H. Warner, The identification of inner tube defects in double-wall carbon nanotubes, Small. 8 (2012) 3810–3815. doi:10.1002/smll.201201625.

[7] J.W.G. Wilder, L.C. Venema, A.G. Rinzler, R.E. Smalley, C. Dekker, Electronic structure of atomically resolved carbon nanotubes, Nature. 391 (1998) 59–62. doi:10.1038/34139.

[8] T.W. Odom, J.L. Huang, P. Kim, C.M. Lieber, Atomic structure and electronic properties of single-walled carbon nanotubes, Nature. 391 (1998) 62–64. doi:10.1038/34139.

[9] Venema, L. Venema, V. Meunier, P. Lambin, C. Dekker, Venema, Atomic structure of carbon nanotubes from scanning tunneling microscopy, Phys. Rev. B. 61 (2000) 2991–2996. doi:10.1103/PhysRevB.61.2991.

[10] J.C. Meyer, M. Paillet, G.S. Duesberg, S. Roth, Electron diffraction analysis of individual single-walled carbon nanotubes., Ultramicroscopy. 106 (2006) 176–90. doi:10.1016/j.ultramic.2005.07.008.

[11] L.-C. Qin, Determination of the chiral indices (n,m) of carbon nanotubes by electron diffraction., Phys. Chem. Chem. Phys. 9 (2007) 31–48. doi:10.1039/b614121h.

[12] S. Amelinckx, A. Lucas, P. Lambin, Electron diffraction and microscopy of nanotubes, Reports Prog. Phys. 62 (1999) 1471–1524. doi:10.1088/0034-4885/62/11/201.

[13] H. Jiang, A.G. Nasibulin, D.P. Brown, E.I. Kauppinen, Unambiguous atomic structural determination of single-walled carbon nanotubes by electron diffraction, Carbon N. Y. 45 (2007) 662–667. doi:10.1016/j.carbon.2006.07.025.

[14] Z. Liu, Q. Zhang, L.-C.C. Qin, Accurate determination of atomic structure of multiwalled carbon nanotubes by nondestructive nanobeam electron diffraction, Appl. Phys. Lett. 86 (2005) 191903. doi:10.1063/1.1923170.

[15] R. Arenal, P. Löthman, M. Picher, T. Than, M. Paillet, V. Jourdain, Direct evidence of atomic structure conservation along ultra-long carbon nanotubes, J. Phys. Chem. C. 116 (2012) 14103–14107. doi:10.1021/jp212540n.

[16] R. Arenal, M. Kociak, A. Loiseau, D.J. Miller, Determination of chiral indices of individual single- And double-walled boron nitride nanotubes by electron diffraction, Appl. Phys. Lett. 89 (2006). doi:10.1063/1.2335379.

[17] K. Hirahara, M. Kociak, S. Bandow, T. Nakahira, K. Itoh, Y. Saito, S. Iijima, Chirality

correlation in double-wall carbon nanotubes as studied by electron diffraction, Phys. Rev. B. 73 (2006) 195420. doi:10.1103/PhysRevB.73.195420.

[18] S.M. Bachilo, M.S. Strano, C. Kittrell, R.H. Hauge, R.E. Smalley, R.B. Weisman, Structure-assigned optical spectra of single-walled carbon nanotubes., Science. 298 (2002) 2361–2366. doi:10.1126/science.1078727.

[19] M.Y. Sfeir, F. Wang, L. Huang, C.-C. Chuang, J. Hone, S.P. O'brien, T.F. Heinz, L.E. Brus, Probing electronic transitions in individual carbon nanotubes by Rayleigh scattering., Science. 306 (2004) 1540–1543. doi:10.1126/science.1103294.

[20] S. Berciaud, C. Voisin, H. Yan, B. Chandra, R. Caldwell, Y. Shan, L.E. Brus, J. Hone, T.F. Heinz, Excitons and high-order optical transitions in individual carbon nanotubes: A Rayleigh scattering spectroscopy study, Phys. Rev. B. 81 (2010) 41414. doi:10.1103/PhysRevB.81.041414.

[21] K. Liu, J. Deslippe, F. Xiao, R.B. Capaz, X. Hong, S. Aloni, A. Zettl, W. Wang, X. Bai, S.G. Louie, E. Wang, F. Wang, An atlas of carbon nanotube optical transitions., Nat. Nanotechnol. 7 (2012) 325–9. doi:10.1038/nnano.2012.52.

[22] J.-C. Blancon, M. Paillet, H.N. Tran, X.T. Than, S.A. Guebrou, A. Ayari, A. San Miguel, N.-M. Phan, A.-A. Zahab, J.-L. Sauvajol, N. Del Fatti, F. Vallée, Direct measurement of the absolute absorption spectrum of individual semiconducting single-wall carbon nanotubes., Nat. Commun. 4 (2013) 2542. doi:10.1038/ncomms3542.

[23] A. Jorio, C. Fantini, M. a. Pimenta, R.B. Capaz, G.G. Samsonidze, G. Dresselhaus, M.S. Dresselhaus, J. Jiang, N. Kobayashi, A. Grüneis, R. Saito, Resonance Raman spectroscopy (n,m)-dependent effects in small-diameter single-wall carbon nanotubes, Phys. Rev. B - Condens. Matter Mater. Phys. 71 (2005) 1–11. doi:10.1103/PhysRevB.71.075401.

[24] H. Telg, J. Maultzsch, S. Reich, F. Hennrich, C. Thomsen, Chirality Distribution and Transition Energies of Carbon Nanotubes, Phys. Rev. Lett. 93 (2004) 177401. doi:10.1103/PhysRevLett.93.177401.

[25] C. Fantini, A. Jorio, M. Souza, M. Strano, M. Dresselhaus, M. Pimenta, Optical Transition Energies for Carbon Nanotubes from Resonant Raman Spectroscopy: Environment and Temperature Effects, Phys. Rev. Lett. 93 (2004) 147406. doi:10.1103/PhysRevLett.93.147406.

[26] J.C. Meyer, M. Paillet, T. Michel, A. Moréac, A. Neumann, G.S. Duesberg, S. Roth, J.-L.L. Sauvajol, Raman Modes of Index-Identified Freestanding Single-Walled Carbon Nanotubes, Phys. Rev. Lett. 95 (2005) 217401. doi:10.1103/PhysRevLett.95.217401.

[27] T. Michel, M. Paillet, a Zahab, D. Nakabayashi, V. Jourdain, R. Parret, J.-L. Sauvajol, About the indexing of the structure of single-walled carbon nanotubes from resonant Raman scattering, Adv. Nat. Sci. Nanosci. Nanotechnol. 1 (2010) 45007. doi:10.1088/2043-6262/1/4/045007.

[28] M. Paillet, T. Michel, A. Zahab, D. Nakabayashi, V. Jourdain, R. Parret, J. Meyer, J.-L. Sauvajol, Probing the structure of single-walled carbon nanotubes by resonant Raman scattering, Phys. Status Solidi. 247 (2010) 2762–2767. doi:10.1002/pssb.201000147.

[29] K. Liu, C. Jin, X. Hong, J. Kim, A. Zettl, E. Wang, F. Wang, Van der Waals-coupled electronic states in incommensurate double-walled carbon nanotubes, Nat. Phys. (2014). doi:10.1038/nphys3042.

[30] M.Y. Sfeir, T. Beetz, F. Wang, L. Huang, X.M.H. Huang, M. Huang, J. Hone, S.O. Brien, J.A. Misewich, T.F. Heinz, L. Wu, Y. Zhu, L.E. Brus, S. O'Brien, J.A. Misewich, T.F. Heinz, L. Wu, Y. Zhu, L.E. Brus, Optical Spectroscopy of Individual Single-Walled

Carbon Nanotubes of Defined Chiral Structure, Science. 312 (2006) 554–556. doi:10.1126/science.1124602.

[31] D. Levshov, T.X. Than, R. Arenal, V.N. Popov, R. Parret, M. Paillet, V. Jourdain, A.A. Zahab, T. Michel, Y.I. Yuzyuk, J.-L.L. Sauvajol, Experimental evidence of a mechanical coupling between layers in an individual double-walled carbon nanotube., Nano Lett. 11 (2011) 4800–4. doi:10.1021/nl2026234.

[32] D. Levshov, T. Michel, T. Than, M. Paillet, R. Arenal, V. Jourdain, Y.I. Yuzyuk, J.-L. Sauvajol, Comparative Raman Study of Individual Double-Walled Carbon Nanotubes and Single-Walled Carbon Nanotubes, J. Nanoelectron. Optoelectron. 8 (2013) 9–15. doi:10.1166/jno.2013.1423.

[33] D. Levshov, T. Michel, M. Paillet, X.T. Than, H.N. Tran, R. Arenal, A. Rahmani, M. Boutahir, A.-A. Zahab, J.-L. Sauvajol, Coupled Vibrations in Index-Identified Carbon Nanotubes, MRS Proc. 1700 (2014) 69–77. doi:10.1557/opl.2014.574.

[34] K. Liu, X. Hong, M. Wu, F. Xiao, W. Wang, X. Bai, J.W. Ager, S. Aloni, A. Zettl, E. Wang, F. Wang, Quantum-coupled radial-breathing oscillations in double-walled carbon nanotubes., Nat. Commun. 4 (2013) 1375. doi:10.1038/ncomms2367.

[35] D.I. Levshov, T. Michel, R. Arenal, H.N. Tran, T.X. Than, M. Paillet, Y.I. Yuzyuk, J.-L. Sauvajol, Interlayer Dependence of G-Modes in Semiconducting Double-Walled Carbon Nanotubes, J. Phys. Chem. C. 119 (2015) 23196–23202. doi:10.1021/acs.jpcc.5b05888.

[36] D.I. Levshov, M. V Avramenko, X. Than, T. Michel, R. Arenal, M. Paillet, D. V Rybkovskiy, A. V Osadchy, S.B. Rochal, Y.I. Yuzyuk, J. Sauvajol, Study of collective radial breathing-like modes in double-walled carbon nanotubes: combination of continuous two-dimensional membrane theory and Raman spectroscopy, J. Nanophotonics. 10 (2016) 12502. doi:10.1117/1.JNP.10.012502.

[37] a. Débarre, M. Kobylko, a. M. Bonnot, a. Richard, V.N. Popov, L. Henrard, M. Kociak, Electronic and Mechanical Coupling of Carbon Nanotubes: A Tunable Resonant Raman Study of Systems with Known Structures, Phys. Rev. Lett. 101 (2008) 1–4. doi:10.1103/PhysRevLett.101.197403.

[38] T. Michel, M. Paillet, D. Nakabayashi, M. Picher, V. Jourdain, J.C. Meyer, a. a. Zahab, J.-L. Sauvajol, Indexing of individual single-walled carbon nanotubes from Raman spectroscopy, Phys. Rev. B. 80 (2009) 245416. doi:10.1103/PhysRevB.80.245416.

[39] J.C. Meyer, M. Paillet, S. Roth, Single-Molecule Torsional Pendulum, Science (80-.). 309 (2005) 1539–1542. doi:10.1126/science.1115067.

[40] M. Kociak, K. Suenaga, K. Hirahara, Y. Saito, T. Nakahira, S. Iijima, Linking chiral indices and transport properties of double-walled carbon nanotubes., Phys. Rev. Lett. 89 (2002) 155501. doi:10.1103/PhysRevLett.89.155501.

[41] P. Myllyperkio, O. Herranen, J. Rintala, H. Jiang, P.R. Mudimela, Z. Zhu, A.G. Nasibulin, A. Johansson, E.I. Kauppinen, M. Ahlskog, M. Pettersson, Femtosecond Four-Wave-Mixing, ACS Nano. 4 (2010) 6780.

[42] S. Huang, X. Cai, J. Liu, Growth of millimeter-long and horizontally aligned single-walled carbon nanotubes on flat substrates, J. Am. Chem. Soc. 125 (2003) 5636–5637. doi:10.1021/ja034475c.

[43] T.X. Tinh, N. Van Chuc, V. Jourdain, M. Paillet, D.-Y. Kim, J.-L. Sauvajol, N.T.T. Tam, P.N. Minh, Synthesis of individual ultra-long carbon nanotubes and transfer to other substrates, J. Exp. Nanosci. 6 (2011) 547–556. doi:10.1080/17458080.2010.498839.

[44] L.-C. Qin, Electron diffraction from carbon nanotubes, Reports Prog. Phys. 69 (2006) 2761–2821. doi:10.1088/0034-4885/69/10/R02.

[45] A.A. Lucas, P. Lambin, Diffraction by DNA, carbon nanotubes and other helical nanostructures, Reports Prog. Phys. 68 (2005) 1181–1249. doi:10.1088/0034-4885/68/5/R05.

[46] M. Kociak, K. Hirahara, K. Suenaga, S. Iijima, How accurate can the determination of chiral indices of carbon nanotubes be?, Eur. Phys. J. B - Condens. Matter. 32 (2003) 457–469. doi:10.1140/epjb/e2003-00127-2.

[47] C.S. Allen, C. Zhang, G. Burnell, A.P. Brown, J. Robertson, B.J. Hickey, A review of methods for the accurate determination of the chiral indices of carbon nanotubes from electron diffraction patterns, Carbon N. Y. 49 (2011) 4961–4971. doi:10.1016/j.carbon.2011.06.100.

[48] H. Jiang, D.P. Brown, P. Nikolaev, A.G. Nasibulin, E.I. Kauppinen, Determination of helicities in unidirectional assemblies of graphitic or graphiticlike tubular structures, Appl. Phys. Lett. 93 (2008) 13–16. doi:10.1063/1.2993217.

[49] H. Deniz, A. Derbakova, L.C. Qin, A systematic procedure for determining the chiral indices of multi-walled carbon nanotubes using electron diffraction-each and every shell, Ultramicroscopy. 111 (2010) 66–72. doi:10.1016/j.ultramic.2010.09.010.

[50] M. Gao, J.M. Zuo, R.D. Twesten, I. Petrov, L.A. Nagahara, R. Zhang, Structure determination of individual single-wall carbon nanotubes by nanoarea electron diffraction, Appl. Phys. Lett. 82 (2003) 2703. doi:10.1063/1.1569418.

[51] H. Jiang, D. Brown, A. Nasibulin, E. Kauppinen, Robust Bessel-function-based method for determination of the (n,m) indices of single-walled carbon nanotubes by electron diffraction, Phys. Rev. B. 74 (2006) 35427. doi:10.1103/PhysRevB.74.035427.

[52] K. Liu, Z. Xu, W. Wang, P. Gao, W. Fu, X. Bai, E. Wang, Direct determination of atomic structure of large-indexed carbon nanotubes by electron diffraction: application to double-walled nanotubes, J. Phys. D. Appl. Phys. 42 (2009) 125412. doi:10.1088/0022-3727/42/12/125412.

[53] L.-C. Qin, Measuring the true helicity of carbon nanotubes, Chem. Phys. Lett. 297 (1998) 23–28. doi:10.1016/S0009-2614(98)01122-1.

[54] Z. Liu, L.C. Qin, A direct method to determine the chiral indices of carbon nanotubes, Chem. Phys. Lett. 408 (2005) 75–79. doi:10.1016/j.cplett.2005.04.016.

[55] R. Arenal, X. Blase, A. Loiseau, Boron-nitride and boron-carbonitride nanotubes: synthesis, characterization and theory, Adv. Phys. 59 (2010) 101–179. doi:10.1080/00018730903562033.

[56] R. Arenal, O. Stephan, Local TEM Spectroscopic Studies on Carbon- and Boron Nitride-Based Nanomaterials, in: F.L. Deepak, A. Mayoral, R. Arenal (Eds.), Adv. Transm. Electron Microsc. Appl. to Nanomater., 1st ed., Springer International Publishing, 2015: p. 272. doi:10.1007/978-3-319-15177-9.

[57] R. Saito, M. Hofmann, G. Dresselhaus, A. Jorio, Raman spectroscopy of graphene and carbon nanotubes, Adv. Phys. 60 (2011) 413–550.

[58] P. Araujo, I. Maciel, P. Pesce, M. Pimenta, S. Doorn, H. Qian, a. Hartschuh, M. Steiner, L. Grigorian, K. Hata, a. Jorio, Nature of the constant factor in the relation between radial breathing mode frequency and tube diameter for single-wall carbon nanotubes, Phys. Rev. B. 77 (2008) 241403. doi:10.1103/PhysRevB.77.241403.

[59] P.T. Araujo, A. Jorio, The role of environmental effects on the optical transition energies and radial breathing mode frequency of single wall carbon nanotubes, Phys. Status Solidi. 245 (2008) 2201–2204. doi:10.1002/pssb.200879625.

[60] K. Liu, W. Wang, M. Wu, F. Xiao, X. Hong, S. Aloni, X. Bai, E. Wang, F. Wang, Intrinsic radial breathing oscillation in suspended single-walled carbon nanotubes, Phys. Rev. B - Condens. Matter Mater. Phys. 83 (2011) 1–4. doi:10.1103/PhysRevB.83.113404.

[61] R.A. Jishi, L. Venkataraman, M.S. Dresselhaus, G. Dresselhaus, Phonon modes in carbon nanotubules, Chem. Phys. Lett. 209 (1993) 77–82. doi:10.1016/0009-2614(93)87205-H.

[62] J. Kürti, G. Kresse, H. Kuzmany, J. Kurti, First-principles calculations of the radial breathing mode of single-wall carbon nanotubes, Phys. Rev. B. 58 (1998) 8869–8872. doi:10.1103/PhysRevB.58.R8869.

[63] G. Mahan, Oscillations of a thin hollow cylinder: Carbon nanotubes, Phys. Rev. B. 65 (2002) 235402. doi:10.1103/PhysRevB.65.235402.

[64] S.B. Rochal, V.L. Lorman, Y.I. Yuzyuk, Two-dimensional elasticity determines the low-frequency dynamics of single- and double-walled carbon nanotubes, Phys. Rev. B. 88 (2013) 235435. doi:10.1103/PhysRevB.88.235435.

[65] M. Paillet, T. Michel, J.C. Meyer, V.N. Popov, L. Henrard, S. Roth, J.L. Sauvajol, Raman active phonons of identified semiconducting single-walled carbon nanotubes, Phys. Rev. Lett. 96 (2006) 1–4. doi:10.1103/PhysRevLett.96.257401.

[66] T. Michel, M. Paille, J.C. Meyer, V.N. Popov, L. Henrard, P. Poncharal, A. Zahab, J.L. Sauvajol, Raman spectroscopy of (n,m)-identified individual single-walled carbon nanotubes, Phys. Status Solidi Basic Res. 244 (2007) 3986–3991. doi:10.1002/pssb.200776177.

[67] S. Chiashi, K. Kono, D. Matsumoto, J. Shitaba, N. Homma, A. Beniya, T. Yamamoto, Y. Homma, Adsorption effects on radial breathing mode of single-walled carbon nanotubes, Phys. Rev. B - Condens. Matter Mater. Phys. 91 (2015) 1–5. doi:10.1103/PhysRevB.91.155415.

[68] Y. Homma, S. Chiashi, T. Yamamoto, K. Kono, D. Matsumoto, J. Shitaba, S. Sato, Photoluminescence measurements and molecular dynamics simulations of water adsorption on the hydrophobic surface of a carbon nanotube in water vapor, Phys. Rev. Lett. 110 (2013) 1–4. doi:10.1103/PhysRevLett.110.157402.

[69] M. V. Avramenko, S.B. Rochal, Y.I. Yuzyuk, Symmetry of the carbon nanotube modes and their origin from the phonon branches of graphene, Phys. Rev. B - Condens. Matter Mater. Phys. 87 (2013) 35407. doi:10.1103/PhysRevB.87.035407.

[70] R. Saito, T. Takeya, T. Kimura, G. Dresselhaus, M. Dresselhaus, Raman intensity of single-wall carbon nanotubes, Phys. Rev. B. 57 (1998) 4145–4153. doi:10.1103/PhysRevB.57.4145.

[71] H. Telg, J.G. Duque, M. Staiger, X. Tu, F. Hennrich, M.M. Kappes, M. Zheng, J. Maultzsch, C. Thomsen, S.K. Doorn, Chiral index dependence of the G+ and G- Raman modes in semiconducting carbon nanotubes., ACS Nano. 6 (2012) 904–11. doi:10.1021/nn2044356.

[72] S. Brown, A. Jorio, P. Corio, M. Dresselhaus, G. Dresselhaus, R. Saito, K. Kneipp, Origin of the Breit-Wigner-Fano lineshape of the tangential G-band feature of metallic carbon nanotubes, Phys. Rev. B. 63 (2001) 155414. doi:10.1103/PhysRevB.63.155414.

[73] S. Piscanec, M. Lazzeri, J. Robertson, A. Ferrari, F. Mauri, Optical phonons in carbon nanotubes: Kohn anomalies, Peierls distortions, and dynamic effects, Phys. Rev. B. 75 (2007) 35427. doi:10.1103/PhysRevB.75.035427.

[74] O. Dubay, G. Kresse, Accurate density functional calculations for the phonon dispersion relations of graphite layer and carbon nanotubes, Phys. Rev. B. 67 (2003) 35401. doi:10.1103/PhysRevB.67.035401.

[75] V.N. Popov, P. Lambin, Radius and chirality dependence of the radial breathing mode and the G -band phonon modes of single-walled carbon nanotubes, Phys. Rev. B - Condens. Matter Mater. Phys. 73 (2006) 1–9. doi:10.1103/PhysRevB.73.085407.

[76] J.G. Duque, H. Telg, H. Chen, A.K. Swan, A.P. Shreve, X. Tu, M. Zheng, S.K. Doorn, Quantum interference between the third and fourth exciton states in semiconducting carbon nanotubes using resonance Raman spectroscopy, Phys. Rev. Lett. 108 (2012) 1–5. doi:10.1103/PhysRevLett.108.117404.

[77] L.G. Moura, M.V.O. Moutinho, P. Venezuela, C. Fantini, A. Righi, M.S. Strano, M.A. Pimenta, Raman excitation profile of the G band in single-chirality carbon nanotubes, Phys. Rev. B - Condens. Matter Mater. Phys. 89 (2014) 35402. doi:10.1103/PhysRevB.89.035402.

[78] J.G. Duque, H. Chen, A.K. Swan, A.P. Shreve, S. Kilina, S. Tretiak, X. Tu, M. Zheng, S.K. Doorn, Violation of the condon approximation in semiconducting carbon nanotubes, ACS Nano. 5 (2011) 5233–5241. doi:10.1021/nn201430z.

[79] T. Michel, M. Paillet, J.C. Meyer, V.N. Popov, L. Henrard, J.L. Sauvajol, E33 and E44 optical transitions in semiconducting single-walled carbon nanotubes: Electron diffraction and Raman experiments, Phys. Rev. B - Condens. Matter Mater. Phys. 75 (2007) 1–5. doi:10.1103/PhysRevB.75.155432.

[80] V. Popov, L. Henrard, Comparative study of the optical properties of single-walled carbon nanotubes within orthogonal and nonorthogonal tight-binding models, Phys. Rev. B. 70 (2004) 115407. doi:10.1103/PhysRevB.70.115407.

[81] V.N. Popov, Curvature effects on the structural , electronic and optical properties of isolated single-walled carbon nanotubes within a symmetry-adapted non-orthogonal tight-binding model, New J. Phys. 6 (2004) 17. doi:10.1088/1367-2630/6/1/017.

[82] R. Parret, D. Levshov, T.X. Than, D. Nakabayashi, T. Michel, M. Paillet, R. Arenal, V.N. Popov, V. Jourdain, Y.I. Yuzyuk, A.A. Zahab, J.-L. Sauvajol, Raman Spectroscopy on Individual Identified Carbon Nanotubes, MRS Proc. 1407 (2012) mrsf11-1407-aa07-01. doi:10.1557/opl.2012.464.

[83] M. Hanfland, H. Beister, K. Syassen, Graphite under pressure: Equation of state and first-order Raman modes, Phys. Rev. B. 39 (1989) 12598–12603. doi:10.1103/PhysRevB.39.12598.

[84] D. Christofilos, J. Arvanitidis, G.A. Kourouklis, S. Ves, T. Takenobu, Y. Iwasa, H. Kataura, Identification of inner and outer shells of double-wall carbon nanotubes using high-pressure Raman spectroscopy, Phys. Rev. B - Condens. Matter Mater. Phys. 76 (2007) 113402. doi:10.1103/PhysRevB.76.113402.

[85] T.C. Hirschmann, P.T. Araujo, H. Muramatsu, X. Zhang, K. Nielsch, Y.A. Kim, M.S. Dresselhaus, Characterization of bundled and individual triple-walled carbon nanotubes by resonant Raman spectroscopy., ACS Nano. 7 (2013) 2381–7. doi:10.1021/nn3055708.

[86] S. Bandow, M. Takizawa, K. Hirahara, M. Yudasaka, S. Iijima, Raman scattering study of double-wall carbon nanotubes derived from the chains of fullerenes in single-wall carbon nanotubes, Chem. Phys. Lett. 337 (2001) 48–54. doi:10.1016/S0009-2614(01)00192-0.

[87] H. Qiu, Z. Shi, Z. Gu, J. Qiu, Controllable preparation of triple-walled carbon nanotubes and their growth mechanism., Chem. Commun. (Camb). 2 (2007) 1092–4. doi:10.1039/b615265a.

[88] V. Popov, L. Henrard, Breathinglike phonon modes of multiwalled carbon nanotubes, Phys. Rev. B. 65 (2002) 235415. doi:10.1103/PhysRevB.65.235415.